



ELSEVIER

Contents lists available at ScienceDirect

International Journal of Engineering Science

journal homepage: www.elsevier.com/locate/ijengsci

Full Length Article

Modeling and experimental analysis of piezoresistive behavior in conductive porous elastomer under significantly large deformation

Jianpeng Zhang^a, Song Wei^a, Chao Shang^a, Yu Duan^a, Zhaoqiang He^a, Hua An^a, Xinge Yu^b, Zhengchun Peng^{a,*}

^a State Key Laboratory of Radio Frequency Heterogeneous Integration (Shenzhen University), School of Physics and Optoelectronic Engineering, Shenzhen University, Shenzhen, Guangdong, China

^b Department of Biomedical Engineering, City University of Hong Kong, Hong Kong, China

ARTICLE INFO

Keywords:

Piezoresistive model, Buckling deformation, Bidirectional piezoresistive phenomenon, Resistance overshooting behavior

ABSTRACT

Piezoresistive porous elastomers (PPEs) are gaining attention in the field of flexible electronics due to their unique properties including ultra softness, ultra lightness, and high sensitivity. These properties can be precisely adjusted through advanced material synthesis and micro/nano-fabrication technologies that control the size, shape, and composition of the functional nanoparticles. Despite various theoretical models of porous materials developed to advance the design of these materials, issues such as reverse piezoresistive response and resistance overshooting remains to be unsolved. Using principles of elastic mechanics and electrical tunnel effects, the present study introduces an analytical model that considers the effects of multimodal buckling of the pore wall, pore closure, microcracks, and mismatch within the pore wall under large deformation. The proposed model achieves a 99.5 % accuracy rate in describing the piezoresistive response (stress and resistance) under 75 % compression deformation by incorporating electrical tunnel theory into the mechanical model. The study also uncovers the mechanism behind high resistance overshooting and its relevant influences, including factors such as loading speed and application temperature. These findings are expected to drive the development of better porous composites and pave the way for practical applications of PPEs in various fields of smart sensors.

1. Introduction

Piezoresistive porous elastomers (PPEs) are a promising class of materials that offer unique combinations of properties, such as high sensitivity, ultrasoft, light, and low cost for pressure sensing applications, as well as the ability to respond to both mechanical and magnetic stimuli (Zhang et al., 2022; Li et al., 2021; Zhao et al., 2021). PPEs are typically composed of a porous elastomer such as thermoplastic polyether urethanes (TPU) (Gu et al., 2023), polydimethylsiloxane (PDMS) (Prabagar et al., 2023), fluoroelastomer (FKM) (Ma et al., 2022), and melamine formaldehyde resin (MF) (Wang et al., 2023), combined with small nanoparticles such as carbon black (CB) or silver (Nan et al., 2023). The nanoparticle dispersion can be either within the elastomer or distributed on the surface of the pore walls (Fu et al., 2023; Lv et al., 2023). Current research efforts focus on unlocking new ways to optimize the

* Corresponding author.

E-mail address: zcpeng@szu.edu.cn (Z. Peng).

<https://doi.org/10.1016/j.ijengsci.2024.104091>

Received 25 July 2023; Received in revised form 30 March 2024; Accepted 5 May 2024

Available online 25 May 2024

0020-7225/© 2024 Elsevier Ltd. All rights are reserved, including those for text and data mining, AI training, and similar technologies.

Nomenclature

λ	Compression ratio
R	Resistance
R_0	Initial resistance
μ	Poisson ratio
ρ	Electrical resistivity
χ	Relative density of PPE
α	Tilt angle of beams in OC model
η	Slenderness ratio of the beam
t	Side length of the cross-section
L	Length of the beam
F_x and F_y	Forces along the x-direction and y-direction
F_r	Resultant force
(x, y, z)	Cartesian coordinates
M	Bending moment in the z-direction
M_L	Bending moment at the free end
$(x_m, -y_m)$	Coordinates of the free end
φ	Angle of the resultant force along the x-direction
s	Local coordinate of the beam
θ	Angle of the cross-section along s
I	Moment of inertia of the cross-section
E	Young's modulus
θ^*	Absolute value of the cross-section angle of the inflection point
C	Constant to be determined
n	Number of inflection points of the flexure
U	Potential
J	Electrical current density
A_c	Equivalent area
X	Undetermined parameter depending on the doping of conductive particles
ρ_0	Electrical resistivity of conductive fillers
b	Mass of the charge carriers
$V(T)$	Temperature-modified barrier height
d	Distance between conductive particles
d_0	Initial distance between conductive particles
ϕ	Volume fraction of conductive fillers
ζ	Proportionality coefficient
β	Index of correlation
ε	Strain
f_b	Boltzmann function with a sigmoidal curve
λ_0	Transition center of Boltzmann function
w	Transition constant
$\bar{\sigma}$	Equivalent stress
\bar{R}	Equivalent resistance
f_c	Exponential decay function
τ	Free parameters contingent upon the rate of pore closure
A	Relative resistivity of a solid containing fully closed pores
G	Shear modulus
a	Unconstrained parameter
c_1 and c_2	Free parameters of compressed stress
δ_t	Transverse deformation
L'	Deformed length of a beam
F_v	Vertical force
ν	Parameter representing the changing trend of cracks
\tilde{f}_b	Boltzmann function during creep
\tilde{f}_c	Exponential decay function during creep
\tilde{w} and \tilde{w}_c	Transition constant of Boltzmann function during creep
$\tilde{\tau}$	Free parameters contingent upon the rate of pore closure during creep

Abreviation

PPE	Piezoresistive porous elastomer
TPU	Thermoplastic polyether urethanes
FKM	Fluoroelastomer
PDMS	Polydimethylsiloxane
MF	Melamine formaldehyde resin
CB	Carbon black
E-skin	Electronic skin
PPN	Porous piezoresistive nanocomposite
PF	Piezoresistive foam
GA	Gibson and Ashby
OC	Octadecagon
FCC	Face-centered cubic
BCC	Body-centered cubic
HCP	Hexagonal close-packed
EAC	Ethyl acetate
DMF	N,N-dimethylformamide
SEM	Scanning electron microscope
FEA	Finite element analysis
ADAM	Adaptive moment estimation
PFTN	Porous fluoroelastomer- thermoplastic polyether urethanes nanocomposite
PTN	Porous thermoplastic polyether urethanes nanocomposite
PFN	Porous fluoroelastomer nanocomposite
UMAT	User-material subroutine

composition and structure of these materials to achieve even higher performance and expand the range of potential applications (Lv et al., 2023; Shi et al., 2022).

The presence of porous structures in materials offers several desirable properties, such as low weight, ultra softness, high compressibility, and high piezoresistive sensitivity (Shi et al., 2022; Li et al., 2021; Meena & Sankar, 2021). Materials with these properties are particularly suitable for applications in electronic skin (E-skin), where they can conform to human skin more effectively (Zarei et al., 2023). They are also useful in biomedical engineering, where they can be used to create biomimetic tissues and organs, bone implants, and medical scaffolds (Lv et al., 2021). However, due to the presence of porous structures, their mechanical and electrical properties exhibit complex characteristics, such as non-linear stress-strain responses and intricate piezoresistive properties. Here, we present two typical examples of PPE, such as the compressed porous piezoresistive nanocomposites (PPNs) shown in Fig. 1a and the compressed piezoresistive foams (PFs) shown in Fig. 1b. PPN primarily relies on conductive nanoparticles evenly distributed in the porous elastic matrix to achieve conductivity, whereas PF mainly depends on conductive materials, such as nickel or other metals plated by evaporation or electroplating, or composite conductive materials chemically impregnated, evenly distributed on the surface of the porous skeleton (Zhang et al., 2021; Huang et al., 2022). Figs. 1c and 1d present the piezoresistive behavior of these materials, including the stress-compressibility (stress vs. λ , λ is the ratio of the initial thickness of a substance to its thickness after compression) curves and resistance change ratio-compressibility (R/R_0 vs. λ) curves. The stress-compressibility curve of PF, similar to traditional high-porosity porous materials, exhibits three stages: linear, yield, and exponential (Ashby & Medalist, 1983). In contrast, the stress-compressibility curve of PPN shows only an exponential stage. This difference primarily stems from variations in cellular structures and spatial architectures (Schlumberger & Thommes, 2021). Porous materials possess a distinct skeleton structure, akin to that of PF, along with a uniform spatial distribution. Under a specified pressure, this structure induces buckling of the pore walls, leading to a pronounced yield plateau in the material's behavior (Ashby & Medalist, 1983; Chen & Jin, 2021). Conversely, materials with a graded porosity distribution or stochastic spatial distribution of pores, analogous to PPN, exhibit a lack of a distinct yield plateau due to the random distribution of buckling stresses within the pore wall structure across a range of values (Rahman et al., 2022). To describe the mechanical properties of porous materials, especially elastic porous materials, numerous models have been proposed to capture the diverse compression behaviors observed in different porous structures (Luo et al., 2021). The most well-known model among these is the Gibson and Ashby (GA) model, which simplifies the porous structure into a regular lattice structure and describes the pore walls using a bending beam model (Ashby & Medalist, 1983). The stress-strain compression behavior (elastic, plateau, and densification) of the porous material is captured through the bending and buckling of these beams and the closure of the pore (Ashby & Medalist, 1983). Other similar models include the equal cubic model (Jo & Naguib, 2007), the tetradecahedron model (Kelvin model) (Chen et al., 2017), and the octahedron model (Liu, 2010), collectively recognized as microstructure mechanical models. Concurrently, researchers have proposed phenomenological constitutive models, establishing mathematical correlations between stress and strain derived from empirical data fitting (Goga, 2011). For instance, Rush et al. introduced a phenomenological model based on stress-strain compression phenomena, exhibiting strong fitting capabilities and certain advantages in the identification process compared to the GA model (Rusch, 1970). However, this model lacked precision in describing the densification region. Subsequently, Liu and Subhash proposed a six-parameter constitutive model specifically tailored for polyurethane foam, accommodating linear elasticity, yield plateau, and densification characteristics (Liu & Subhash, 2004). Further advancements in this model were contributed by Avalle et al.

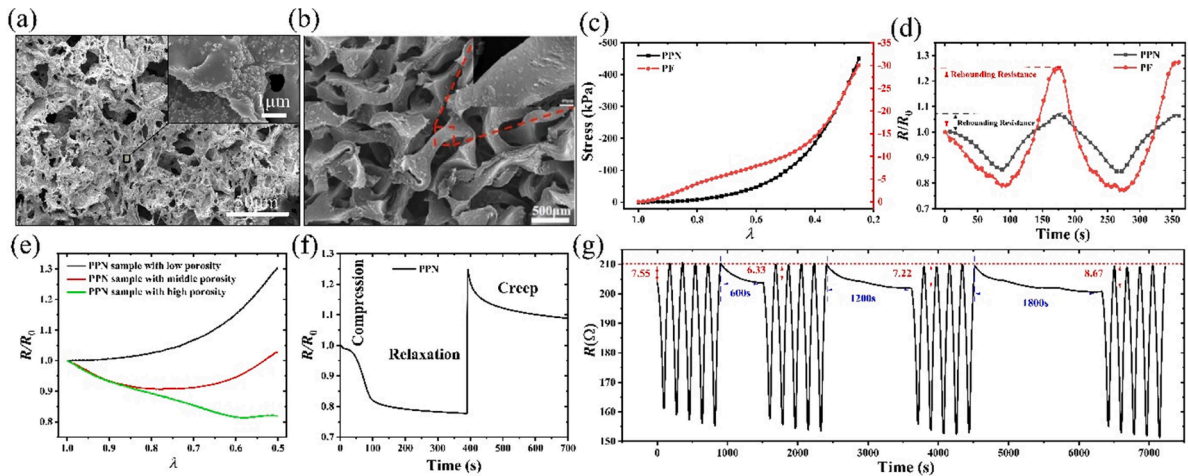


Fig. 1. Piezoresistive behavior of porous piezoresistive elastomers (PPEs). SEM figures of two typical PPEs, including a porous piezoresistive nanocomposite (PPN) (a) and a piezoresistive foam (Huang et al., 2022) (b). Mechanical response (c) and electrical response (d) of two typical PPEs under 75 % compressed strain, with the black line representing PPN and the red line representing PF. (e) Typical resistance sensitivity-compression ratio curves of PPNs with different porosities during the first compression. (f) Relaxation and creep curves of resistance changes with time from a high porosity PPN. (g) Recoverability of overshoot resistance based on a high porosity PPN.

(2007); Goga (2011); Cousins (1976); Sherwood & Frost (1992), and others. Due to the complexity of deformation and evolution within a porous material's internal structure, the mentioned models effectively capture the mechanical behavior of diverse porous materials using a limited set of essential fitting parameters.

The porosity of the matrix plays a crucial role in improving sensor sensitivity by providing channels or void spaces for nanoparticles to move within, increasing their contact with each other, and enhancing the efficiency of electron transport (Ji et al., 2022). For example, Fig. 1d also presents the intrinsic resistance curve of PF and PPN under linear cyclic loading obtained by four-wire methods, which shows a significant resistance overshooting at the first cycle. Additionally, by adjusting the porosity of piezoresistive porous nanocomposites based on TPU matrixes, different piezoresistive curves at first compression can be obtained, as shown in Fig. 1e. The graphical results indicate that both positive and negative piezoresistive features can coexist within a single material system. In the existing definitions of piezoresistive properties, we primarily rely on the increase and decrease of electrical resistance to define positive and negative piezoresistive characteristics, respectively. Increasing the porosity can lead to a change from a positive piezoresistive curve (resistance increasing with compression) to a negative one (resistance decreasing with compression), with the resistance increasing under larger deformation. Nevertheless, the underlying mechanism of porous piezoresistive sensing is intricate, prompting researchers to propose various models to elucidate the intricate principles governing piezoresistive properties. Principally, the tunneling effect prevails, positing that the reduction in electrical resistance arises from the diminished spacing between conductive particles (Kaiser, 2000). Moreover, alterations in geometric structures impacting piezoresistive behavior are encapsulated by $\Delta R/R = (1 + 2\mu) + \Delta\rho/\rho$ (ν is Poisson's ratio) (Vimala & Vandrangi, 2023). In addressing the heightened piezoresistive sensitivity inherent in porous structures, Li et al. conducted a meticulous analysis of cross-sectional images, revealing that the collapse and shrinkage of porous structures contribute to an augmented mutual contact between pore walls, thereby fostering an enriched conductive network within the porous structure (Li et al., 2021). Concurrently, an equivalent network model, which considers the mutual contact of pore walls and incorporates tunneling theory, is introduced for a more comprehensive understanding (Zhang et al., 2017; Zhao et al., 2019). Additionally, Wu et al. proposed that microcrack junctions lead to the disruption of local conductive pathways, resulting in an elevation of electric resistance under small applied strain (Wu et al., 2016). Beyond the quasi-static piezoresistive performance discussed earlier, Fig. 1f illustrates the bulk resistance characteristics of PPN during compression, relaxation, and creep behaviors. It is observed that resistance decreases with relaxation following compressed deformation ($\lambda = 0.5$), implying that internal micro-deformation is linked with resistance. Upon releasing the compression, resistance overshooting indicates that microscopic cracks or mismatches cause an increase in intrinsic resistance during the creep stage. This crack/mismatch is restorable due to resistance reduction at the creep stage. In addition, resistance overshooting during the first cycle can also be restored to its original state as the recovery time increases, as shown in Fig. 1g. Importantly, this overshooting effect persists and does not disappear with multiple compressions. In our earlier investigations, a phenomenological model was introduced as an attempt to elucidate this phenomenon. We posited that within confined compressive deformation, the porous architecture experiences concurrent compressive and tensile deformations. The augmentation of the conductive network is attributed to the compressive component, while tensile deformation in the pore walls induces molecular chain slippage, consequently leading to the breakdown of the conductive network (Zhang et al., 2024). However, extant models lack the precision required to elucidate the microstructural deformation mechanisms of porous elastomers under compression, as well as the nuanced electrical resistance escalation observed under substantial deformations.

To comprehensively elucidate the unconventional piezoresistive phenomenon observed in PPEs under substantial deformation, we developed a novel Octadecagon (OC) cell model. This model, using PPN as an example, elucidates the piezoresistive behaviors of

porous elastomer through a deformation model of beam. The model accounts for large compressed deformation, hyperplastic properties of elastomer matrix, closure of micropore, as well as restorable microcrack and mismatch. In comparison to traditional models such as the GA cell based on face-centered cubic (FCC) and Kevin cell, both the Octahedral cell and Rhombic dodecahedron cell, which are based on body-centered cubic (BCC), follow the hexagonal close-packed (HCP) rule of porogens. This aspect makes the OC cell more compatible with the actual arrangement of porogens, particularly inorganic porogens. To verify the impact of crucial parameters, machine learning was implemented to define these parameters. The study performed extensive experiments on intrinsic piezoresistive behaviors of PPNs to precisely fit the stress and resistance changes during compressed deformation. Additionally, the research identified the effects of buckling of pore wall, closure of pore, and restorable mismatch on positive piezoresistive properties and resistance overshooting. This comprehensive study outlines the first detailed piezoresistive mechanism behind the bidirectional piezoresistive phenomenon and resistance overshooting of PPNs. These findings open new avenues for practical applications and development of flexible electronics, biomedical engineering, sensors, and energy absorbers utilizing porous piezoresistive materials.

2. Piezoresistive model and mechanism of PPNs

2.1. Fabrication of PPNs

The current study employs the sacrificial NaCl templating method (S1) to fabricate PPNs with excellent resistance-strain linear relationships and larger pressure ranges (Zhao et al., 2021). The matrix of PPNs comprises typical linear polymer TPU and typical crosslink polymer FKM, which are dissolved in N,N-dimethylformamide (DMF, Aladdin) solvent and ethyl acetate (EAC) solvent (99.5

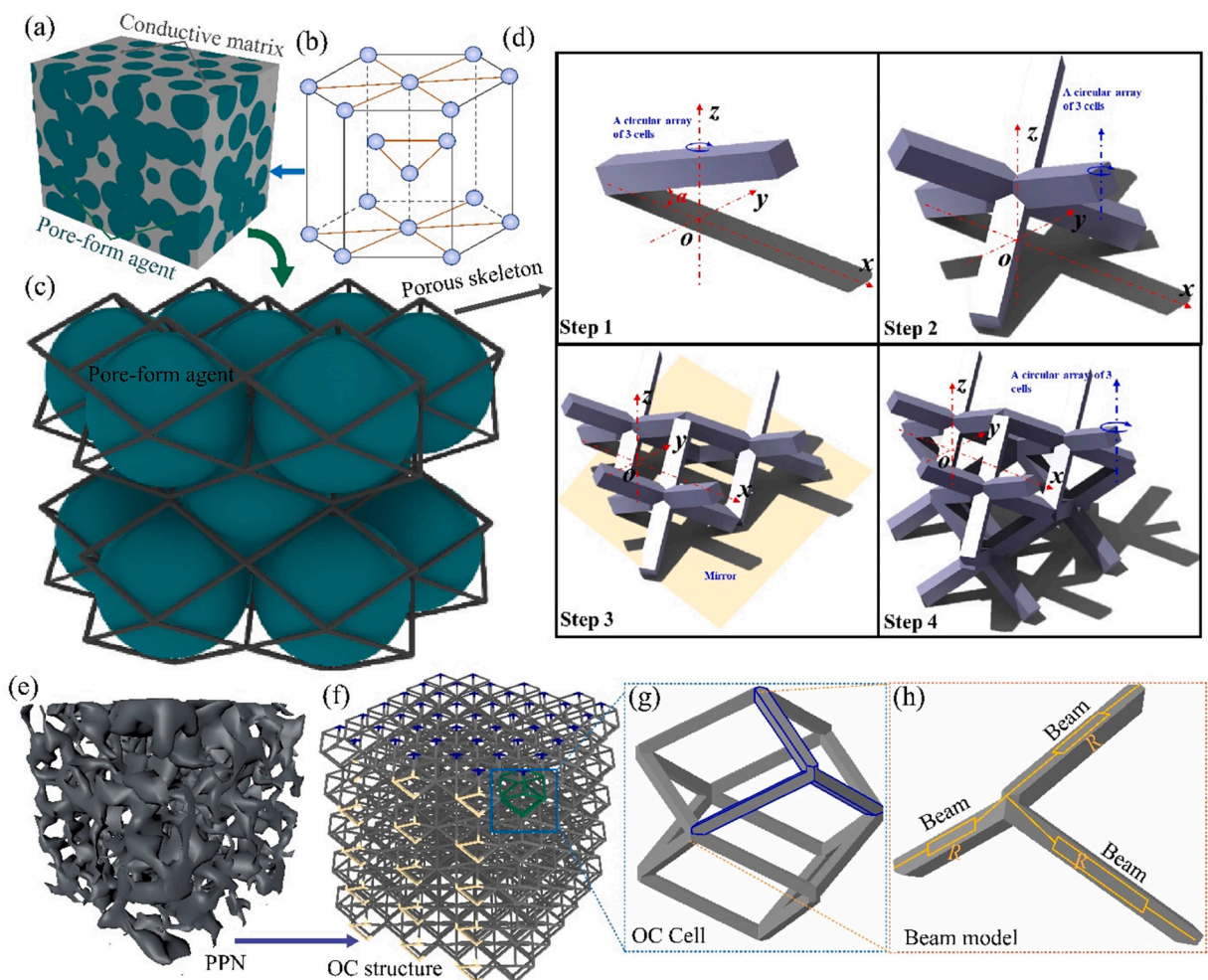


Fig. 2. Octadecagon (OC) cell model. (a) The interactions between the pore-generating agent and the matrix material during the formation of the porous structure. (b) The HCP structure of the pore-generating agent. (c) The OC model, which is based on the HCP structure of the pore-generating agent. (d) The fabrication process of the OC model. (e) Schematic representations of the porous structure. (f) Simplified schematic representations of the periodic OC structures. (g) Schematic representation of an individual OC unit cell. (h) Schematic representation of the equivalent circuit diagram of the beams within the OC unit cell.

%, Aladdin), respectively, as the precursor solution. To enhance the dispersion uniformity, CB nanoparticles are dispersed into EAC solvent (99.5 %, Aladdin) using sonication (JY92-IIDN, SCIENTZ). Planetary ball milling (F-P400, FOCUCY) is used to grind the NaCl sacrifice template into microparticles (~30 μm). Then, NaCl microparticles and CB solvent are mixed into the matrix’s solvent to form the precursor slurry after 30 min of stirring. The precursor slurry is evenly coated on a glass plate and thermally processed to remove organic solvents (DMF and EAC) to form a curing object. Subsequently, immersion of the curing object in water for 12 h ensures complete dissolution of NaCl microparticles, forming the desired PPNs. Finally, a sheet machine (C420, Camoga) and laser cutting machine (UV-3C, Han’s Laser) are employed to control the thickness, width, and length of the dimensional sensor.

2.2. Octadecagon (OC) cell

Conductive nano-fillers can be dispersed effectively in the cell ligament of the polymer matrix for PPNs. Scanning electron microscope (SEM) images of PPNs, displayed in Fig. 1a, show a dense permutation distribution of pores with the hole wall appearing to have a bumpy state due to solvent evaporation. In Fig. 2a, the positional relationship between the porous conductive matrix and the porous pore-form agent during the formation of the porous structure is demonstrated. Due to the absence of relative positional constraints, the pore-form agent exhibits an HCP packing structure, as illustrated in Fig. 2b. Based on the HCP packing structure of the pore-form agent, the OC model is proposed in this study, as illustrated in Fig. 2c. This figure illustrates a detailed representation of the spatial relationship between the pore-form agent and the porous skeleton. The construction process of the OC cell is explained in detail in Fig. 2d. A circular array deformation with three elements was carried out on the central symmetry line, originating from a beam model with a tilt angle of α and a slenderness ratio of η = t/L. Further, a mirror transformation was performed in the horizontal plane based on the circular array transformation to form an OC unit cell. Simultaneously, Fig. 2e shows a schematic representation of the porous structure and its simplified periodic OC unit cell structure (Fig. 2f). Fig. 2g presents a schematic representation of an individual OC unit cell, while Fig. 2h displays the schematic representation of the equivalent circuit diagram of the beams within the OC unit cell. According to the topological structure of the OC cell, the relation between relative density (χ) (the ratio of the density of the porous structure to that of the elastomer matrix) (S2) can be expressed as,

$$\chi = \frac{(6\eta^2 - 4\eta^3)(1 + \tan^2\alpha)^{\frac{3}{2}}}{3\sqrt{3}\tan\alpha} \tag{1}$$

In an unconstrained scenario, it can be observed that the beam elements in the OC cell exhibit flexural buckling mode of deformation at both ends.

Utilizing conductive TPU materials and 3D printing process, a conductive OC cell model is prepared and its equivalent circuit model is displayed in the yellow line in Fig. 3a. Fig. 3b illustrates its quasi-static piezoresistive characteristics under axial compressed deformation (S3). The electrical resistance change curve demonstrates a pattern of initial decrease followed by an increase, resembling the piezoresistive behavior observed in PPN, as illustrated by the red line in Fig. 1e. The compressed force curves of the OC cell show an exponential increase in yield after a linear increase, akin to the stress response of all-directional conductive foam. Additionally, Fig. 3c depicts the compression, relaxation, and creep characteristics of the piezoresistive response of the OC cell, which are similar to the intrinsic resistance response of the PPN. During the relaxation phase, the resistance decreases over time due to a relaxation response to the deformation of the elastomer matrix, as depicted by the red line in Fig. 3c. Upon releasing the compression, the resistance overshooting first shows a step increase and then decreases with time. This observation further suggests that some form of microscopic cracks or mismatch increases the intrinsic resistance during the compressed stage, and this microscopic crack or mismatch is restorable due to the reduction of resistance at the creep stage (Wu et al., 2016).

2.3. Beam model within the OC cell

Fig. 4 displays the structural representation of the beam model of the OC cell. Based on the symmetry of the model in Fig. 2d, each

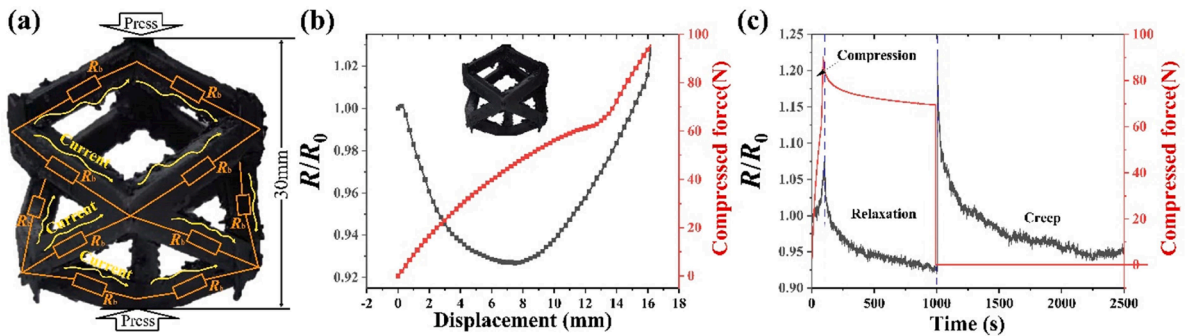


Fig. 3. Piezoresistive behaviors of an OC unit cell. (a) the OC unit cell made by 3D printing technology. (b) Quasi-static piezoresistive behavior of the OC unit cell. (c) Piezoresistive relaxation and creep behaviors of the OC unit cell.

beam can be considered as a perfectly equivalent beam, as depicted by the red lines in Fig. 4a. Fig. 4b illustrates the deformation shape of the beam under compression. Thus, a simplified mechanical model of the beam can be proposed as shown in Fig. 4c. Furthermore, the static equilibrium equations of the beam model can be obtained as,

$$\begin{cases} F_x = -F_r \cos\varphi \\ F_y = -F_r \sin\varphi \\ M = M_L + F_y(x_m - x) + F_x(y_m + y) \end{cases}, \quad (2)$$

where F_x and F_y represent forces along the x-direction and y-direction, respectively. F_r is the resultant force from loading and symmetric conditions. (x, y, z) is Cartesian coordinates. M represents the bending moment in the z-direction, while M_L is the bending moment at the free end. $(x_m, -y_m)$ represents the coordinates of the free end, and φ denotes the direction of the resultant force along the x-direction. Thus, the governing equation under large deformation can be written as

$$\begin{cases} \frac{d\theta}{ds} = \frac{M_L - F_r \sin\varphi(x_m - x) - F_r \cos\varphi(y_m + y)}{EI} \\ \frac{dy}{ds} = \sin\theta \\ \frac{dx}{ds} = \cos\theta \end{cases}, \quad (3)$$

where s is the local coordinate of the beam, and θ is the angle of the cross-section. E represents the effective Young's modulus of the base materials, while $I = t^4 / 12$ denotes the moment of inertia of the cross-section. t is the side length of the square cross-section. Through the differential operation of the first term at Equation (3a), the quadratic differential equation describing the deformation of the beam

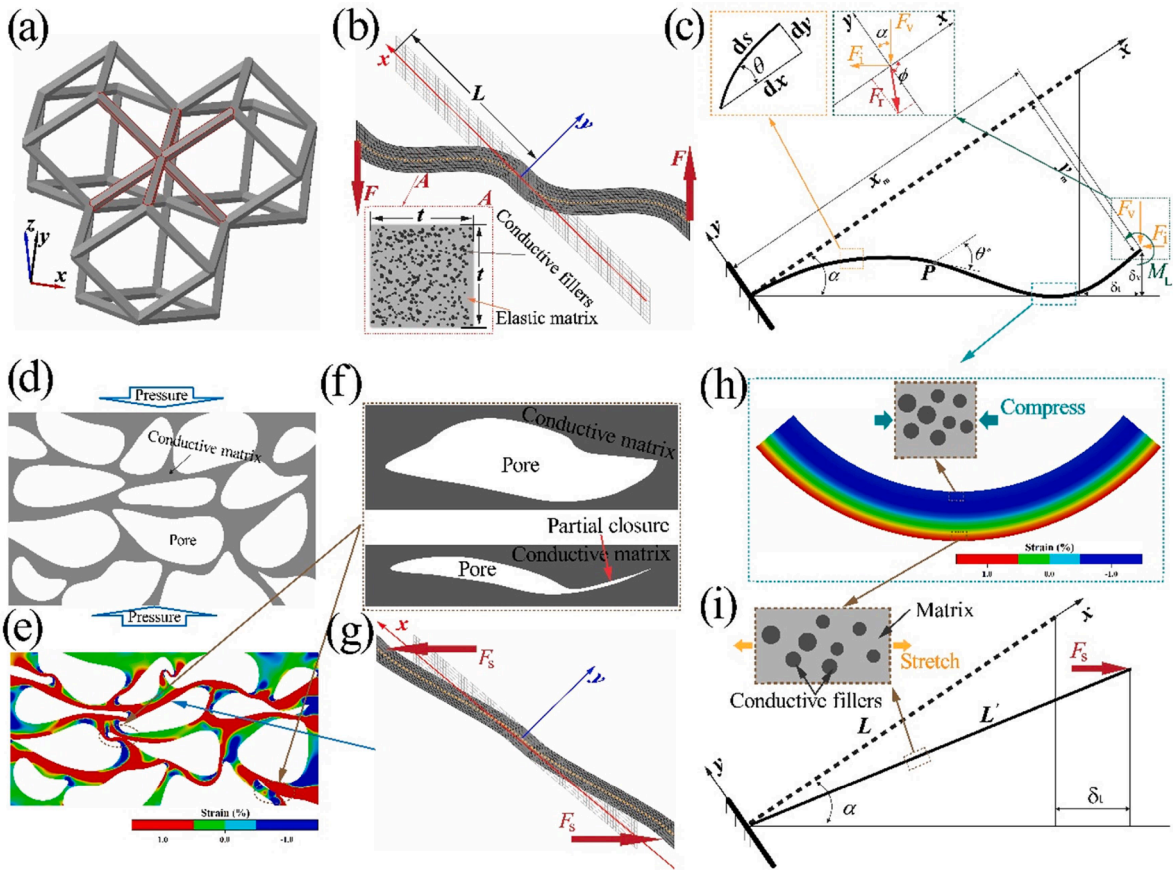


Fig. 4. Beam models describing bending and buckling cell ligaments, closure of pores, and mismatch and microcrack within pore walls. (a) Perfectly equivalent beam within the OC cell. (b) The deformation shape of the beam under compression. (c) A simplified mechanical model of the beam. (d) Schematic representation of a porous structure. (e) Strain distribution contour of the porous structure after compression. (f) Schematic representation of pore closure in the porous structure. (g) Schematic representation of the misalignment and tensile strain generated during uneven pore wall compression. (h) Strain distribution contour caused by pure bending of the beam elements. (i) Simplified mechanical model of mismatch and microcrack within pore wall.

can be written as

$$\frac{d^2\theta}{ds^2} = \frac{F_r \sin\varphi}{EI} \cos\theta - \frac{F_r \cos\varphi}{EI} \sin\theta, \tag{4}$$

2.3.1. Large deflection bending deformation

When the end of the beam is free and the head is fixed, the beam model will produce bending deformation with a large deflection under compression. The boundary condition for this scenario can be written as follows:

$$\begin{cases} s = 0, \theta = 0, x = 0, y = 0 \\ s = L, \theta = 0, x = x_m, y = -y_m \end{cases} \tag{5}$$

If there is an inflection point denoted as P , in which $s = s_0, M = 0$ and $\theta = -\theta^*$. Thus, the undetermined constant C can be obtained as,

$$C = -\frac{F_r}{EI} \cos(\theta^* + \varphi). \tag{6}$$

The transverse free boundary condition at the free hand gives that there is no transverse force loading on the hand, which yields $s\varphi = \pi/2 - \alpha$. Thus,

$$\frac{d\theta}{ds} = \begin{cases} -\sqrt{\frac{2F_r}{EI} \sqrt{\sin(\alpha + \theta) - \sin(\alpha - \theta^*)}}, 0 \leq s \leq s_0 \\ \sqrt{\frac{2F_r}{EI} \sqrt{\sin(\alpha + \theta) - \sin(\alpha - \theta^*)}}, s_0 \leq s \leq L \end{cases} \tag{7}$$

The length of the beam can be obtained as

$$L = \int_{-\theta^*}^0 \frac{2}{\sqrt{\frac{2F_r}{EI} \sqrt{\sin(\alpha + \theta) - \sin(\alpha - \theta^*)}}} d\theta \tag{8}$$

Thus, the angle of the cross-section (θ^*) at the inflection point P can be obtained. Furthermore, the displacement at the free ending of the beam can be obtained as

$$\begin{cases} x_m = \int_{-\theta^*}^0 \frac{2\cos\theta}{\sqrt{\frac{2F_r}{EI} \sqrt{\sin(\alpha + \theta) - \sin(\alpha - \theta^*)}}} d\theta \\ y_m = \int_{-\theta^*}^0 \frac{-2\sin\theta}{\sqrt{\frac{2F_r}{EI} \sqrt{\sin(\alpha + \theta) - \sin(\alpha - \theta^*)}}} d\theta \end{cases}, \tag{9}$$

2.3.2. Buckling deformation with large deflection

According to Eq. (4), The curvature equation of a flexure can be written as

$$\frac{d\theta}{ds} = \pm \sqrt{\frac{2F_r}{EI} \sqrt{\cos(\varphi - \theta) - \cos(\varphi + \theta^*)}} \tag{10}$$

where the plus and minus signs represent the concave-convex relationship of the flexural line. The number of inflection points of the flexure is denoted as n (S4). When n is an even number, the buckling mode exhibits a symmetric buckling mode. When n is an odd number, the buckling mode exhibits an asymmetric buckling mode. Thus, the length of the beam and the displacement condition of the beam head (see Appendix A) can be written as:

$$\begin{cases} L = 2n \int_0^{\theta^*} \frac{1}{\sqrt{\frac{2F_r}{EI} \sqrt{\cos(\varphi - \theta) - \cos(\varphi + \theta^*)}}} d\theta \\ x_m = 2n \int_0^{\theta^*} \frac{\cos\theta}{\sqrt{\frac{2F_r}{EI} \sqrt{\cos(\varphi - \theta) - \cos(\varphi + \theta^*)}}} d\theta \\ y_m = [1 - (-1)^n] \int_0^{\theta^*} \frac{\sin\theta}{\sqrt{\frac{2F_r}{EI} \sqrt{\cos(\varphi - \theta) - \cos(\varphi + \theta^*)}}} d\theta \end{cases} \tag{11}$$

Thus, the compression ratio λ and Poisson ratio μ can be obtained as

$$\lambda = \frac{x_m \sin \alpha - y_m \cos \alpha}{L \sin \alpha}, \quad \mu = \frac{L - x_m - y_m \tan \alpha}{L - x_m + y_m \cot \alpha} \quad (12)$$

2.4. Electrical model

The quasi-static governing equation of potential distribution can be written as

$$\Delta U = -J / \rho \quad (13)$$

where U is the potential, and J is the electrical current density. According to Ohm's Law, the conservation of electrical current at the beam model can be expressed as $\nabla J = 0$. Thus, the equivalent resistance (Arh et al., 2021; Notaros, 2011) can be calculated by

$$R = \int_L \frac{1}{\int_A \rho^{-1} dA_c} dx. \quad (14)$$

The electrical properties of porous nanocomposites are based on conducting filler additives dispersed within insulating matrices forming pore walls. Considering that the behaviors of a single tunnel junction can reasonably describe the conductivity of a composite solid, Ezquerro et al. (Ezquerro et al., 1990) proposed an approximate model to describe its conducting behaviors:

$$\rho = \rho_0 e^{2Xd}, \quad (15)$$

$X = \sqrt{2bV(T)}/h_s \rho_0$ is the electrical resistivity of conductive fillers, b is the mass of the charge carriers, $V(T)$ is the temperature-modified barrier height, d is the distance between conductive particles and is approximately proportional to $\phi^{-1/3}$ (ϕ is the volume fraction of conductive fillers (S2)). In the porous piezoresistive materials formed by inorganic salt pore-forming methods, d can change with porosity due to the microscopic structure formed on the pore wall by solvent evaporation. Besides, the initial distance d_0 between conductive particles depends on the relative density χ , as given by $d_0 = \zeta \chi^{-\beta} \phi^{-1/3}$, where ζ is the proportionality coefficient and β is the index of correlation (S5). Moreover, ε (strain of conductive composite solids) can change d directly and the equivalent resistivity of PPN can be modified as

$$\rho = \rho_0 e^{2Xd_0(1+\varepsilon)} = \rho_0 e^{2X\zeta\chi^{-\beta}\phi^{-1/3}(1+\varepsilon)}. \quad (16)$$

The strain distribution at the beam can be written as

$$\varepsilon_y = -y \frac{d\theta}{dx}. \quad (17)$$

Substituting Eq. (7), (10, 16) and (17) into Eq. (14) yields as,

$$R_{\text{Beam}} = \begin{cases} \frac{\rho_0 L}{t^2} \int_{-\theta^*}^0 \frac{tXd_0}{L \sinh\left(\frac{tXd_0}{2} \sqrt{\frac{2F_r}{EI}} \sqrt{\sin(\alpha + \theta) - \sin(\alpha - \theta^*)}\right)} d\theta, \text{ for bending} \\ \frac{n\rho_0 L}{t^2} \int_{-\theta^*}^0 \frac{tXd_0}{L \sinh\left(\frac{tXd_0}{2} \sqrt{\frac{2F_r}{EI}} \sqrt{\cos(\varphi - \theta) - \cos(\varphi + \theta^*)}\right)} d\theta, \text{ for buckling} \end{cases}, \quad (18)$$

2.5. Weighted superposition principle

Porous materials exhibit a wide range of heterogeneous factors, such as variations in cell size, shape, and thickness of pore walls, which give rise to diverse buckling modals. In Fig. 4d, a finite element analysis (FEA) model depicting a porous structure has been meticulously constructed. This model serves as a foundation for analyzing the mechanical behavior of the porous material under various conditions. Subsequently, Fig. 4e presents the strain distribution contour plot of the porous structure subjected to compressive loading. The intricate pattern of strain distribution visible in the contour plot clearly illustrates the complex deformation behavior exhibited by the pore walls. Specifically, it can be observed that the pore walls undergo a combination of bending deformation and buckling instability, which are key factors governing the overall mechanical response of the porous structure. As a result of pore collapse and pore wall buckling, the mechanical characteristics of porous materials display a yielding-first and hardening-later curve (Huang et al., 2018). The stress curves of PPN represent a transition state from bending mode to buckling mode. It is therefore essential to establish a transition function that accounts for the various buckling models due to the heterogeneity of cells in the material (Grossi et al., 2021; Liu et al., 2022). A Boltzmann function with a sigmoidal curve ($f_b = 1 - (1 + e^{(\lambda - \lambda_0)/w})^{-1}$) is deemed suitable to represent this transition, characterized by a center of transition λ_0 and a transition constant w (Sohrab, 2022). Thus, the equivalent stress $\bar{\sigma}$ and the equivalent resistance \bar{R} (S6) can be expressed as

$$\begin{cases} \bar{\sigma} = f_b \sigma_{\text{bending}} + (1 - f_b) \sigma_{\text{buckling}} \\ \bar{R} = f_b R_{\text{bending}} + (1 - f_b) R_{\text{buckling}} \end{cases} \quad (19)$$

where σ_{bending} , σ_{buckling} , R_{bending} and R_{buckling} are stress and resistance from bending deformation and buckling deformation, respectively.

2.6. Closure of pore and hyper-elastic characteristics of elastomer matrix

The irregular porous structure of the analyzed samples may exhibit partial closure in certain areas when compressed, as illustrated in Fig. 4f. This phenomenon leads to an increase in both the conductive path and the effective modulus, consistent across samples with highly dense porous structures, as predicted by the effective medium theory (Rong et al., 2019; Li et al., 2019). The compression and deformation processes, supported by previous research (Li et al., 2019), reveal that pore collapse increases exponentially and approaches zero as porosity decreases. In this study, an exponential decay function (Zhong-Jie & Gen-Qi, 2012) is utilized to depict the change in resistance, as

$$f_c = 1 - A \left(e^{\frac{-\lambda}{\tau}} - e^{\frac{-1}{\tau}} \right) / \left(1 - e^{\frac{-1}{\tau}} \right). \quad (20)$$

where τ represents the free parameter contingent upon the rate of pore closure and A denotes the relative resistivity of a solid containing fully closed pores. In order to explicate the characteristics of stress variation with deformation, this study employs exponential functions (Rusch, 1970; Storåkers, 1986). By accounting for pore closure, Equation 19 is reformulated as

$$\begin{cases} \sigma = \lambda^{-a} (f_b \sigma_{\text{bending}} + (1 - f_b) \sigma_{\text{buckling}}) \\ R = f_c (f_b R_{\text{bending}} + (1 - f_b) R_{\text{buckling}}) \end{cases}, \quad (21)$$

where parameter a is unconstrained. Additionally, to reconstitute the stress function in Eq. (21), the constitutive stress-deformation relations $\sigma = G(\lambda - \lambda^{-2})$ (where G symbolizes the shear modulus of the matrix) under uniaxial loading conditions within the elastomeric matrix of PPN are considered (Shrimali et al., 2020). Thus, the stress part in Eq. (21) can be rewritten as

$$\sigma = (\lambda^{-c_1} - \lambda^{-c_2}) (f_b \sigma_{\text{bending}} + (1 - f_b) \sigma_{\text{buckling}}), \quad (22)$$

where parameters c_1 and c_2 are free and depend on the structure of the irregular porous material and the elastomeric matrix.

2.7. Recoverable mismatches and microcracks under large deformation

Heterogeneous porous materials can exhibit both bending and buckling modes simultaneously, necessitating a balance between them to maintain stability. To achieve this balance, transverse shear deformation is triggered (Gu et al., 2023), which has little effect on vertical deformation as demonstrated in Fig. 4g. However, the presence of large deformation can also lead to microcracks, causing a decrease in conductivity and an increase in resistance (Han et al., 2020). This phenomenon can be modeled using the tensile deformation of a beam element, as illustrated in Fig. 4i. As a result of the mismatch of transverse deformation δ_t , a deformed length can be calculated using $L' = \sqrt{(L \sin \alpha)^2 + (L \cos \alpha + \delta_t)^2}$. Subsequently, the resistance of the tensile beam can be obtained using $R_{\text{beam}} = (\rho_0 L / t^2) e^{2X d_0 (\sqrt{1 + 2\Delta\mu \cos^2 \alpha + (\Delta\mu \cos \alpha)^2} - 1)}$, where it is noted that the difference of Poisson's ratio between two adjacent cells is denoted by $\Delta\mu = \delta_t / L \cos \alpha$. Due to its high accuracy and excellent flexibility in quantifying material degradation, a modified exponential growth model, a modified exponential growth model (Xu et al., 2022; Su et al., 2023) is introduced to describe recoverable mismatches and microcracks with deformation, characterized by two attributes, λ and t , as given by

$$\Delta\mu = \left(e^{\frac{-\lambda}{\nu}} - e^{\frac{-1}{\nu}} \right) / \left(2 - 2e^{\frac{-1}{\nu}} \right), \quad (23)$$

where parameter ν represents changing trend of cracks and the value is close to 0.5 in the case of limiting compression. In the limit where λ approaches zero, the corresponding $\Delta\mu$ attains a value of 0, indicating pronounced compressibility in the porous material. In this scenario, the deformation primarily involves the bending of pore walls without observable misalignment. Conversely, as λ approaches unity, the $\Delta\mu$ tends towards 0.5, suggesting that materials with closed pores exhibit near-incompressibility. A comprehensive understanding of the intricate mechanical behavior of heterogeneous porous materials is provided by this equation.

2.8. Dimensionless analysis

Utilizing the stress response relation ($\sigma = 2\sqrt{3}F_v / L^2$ and $F_v = F_r \sin(\alpha + \varphi)$) of the cell, the stress-strain of PPN can be written as,

$$\frac{\sigma}{E} = \frac{\sqrt{3}}{3} \eta^4 (\lambda^{-c_1} - \lambda^{-c_2}) \left\{ D_{\text{buckling}}^2 \sin(\alpha + \varphi) + f \left[D_{\text{bending}}^2 - D_{\text{buckling}}^2 \sin(\alpha + \varphi) \right] \right\}. \quad (24)$$

where

$$\begin{cases} D_{\text{bending}} = \int_{-\theta^*}^0 \frac{1}{\sqrt{\sin(\alpha + \theta) - \sin(\alpha - \theta^*)}} d\theta \\ D_{\text{buckling}} = \int_{-\theta^*}^0 \frac{1}{\sqrt{\cos(\varphi - \theta) - \cos(\varphi + \theta^*)}} d\theta \end{cases} \quad (25)$$

Similarly, the resistance response of PPN can be obtained as

$$S = \frac{R_{\text{Beam}}}{R_0} = f_c [f_b C_{\text{bending}} + (1 - f_b) C_{\text{buckling}}] e^{X d_0 M_{\text{Shear}}} \quad (26)$$

where

$$\begin{cases} C_{\text{bending}} = \int_{-\theta^*}^0 \frac{\eta X d_0}{\sinh\left(\frac{D_{\text{TFM}} \eta X d_0}{2} \sqrt{\sin(\alpha + \theta) - \sin(\alpha - \theta^*)}\right)} d\theta \\ C_{\text{buckling}} = \int_{-\theta^*}^0 \frac{n \eta X d_0}{\sinh\left(\frac{D_{\text{TFM}} \eta X d_0}{2} \sqrt{\cos(\varphi - \theta) - \cos(\varphi + \theta^*)}\right)} d\theta \\ M_{\text{Shear}} = \sqrt{1 + 2\Delta\mu \cos^2 \alpha + (\Delta\mu \cos \alpha)^2} - 1 \end{cases} \quad (27)$$

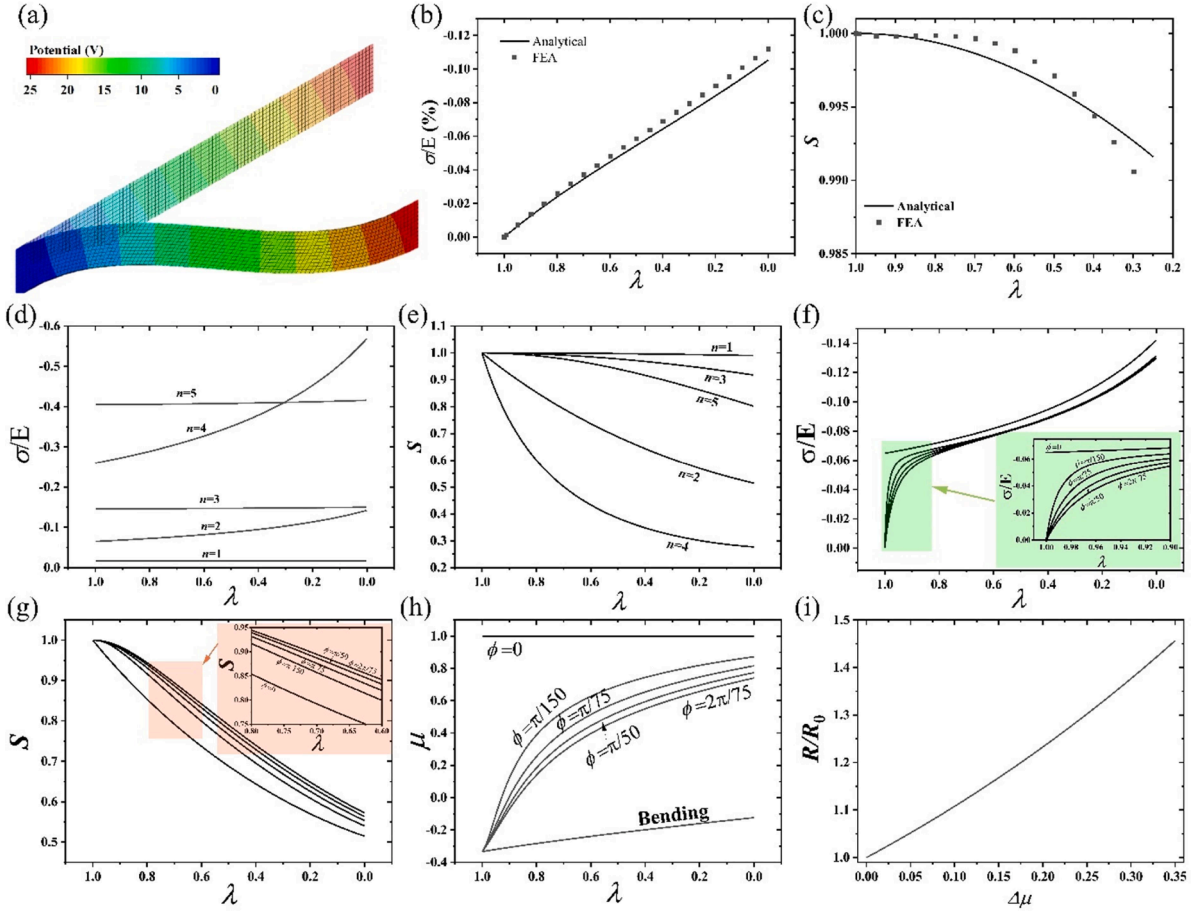


Fig. 5. Analytical results from the beam within OC cell. (a) The potential contours of the beam under bending deformation. The dimensionless stress (b) and sensitivity to deformation (c) of the beam under bending deformation from the FEA and analytical models. The dimensionless stress (d) and sensitivity to deformation (e) of the beam under different buckling modes ($1 \leq n$ and $\varphi = 0$) from the analytical model. Yield characteristics (f) and the sensitivity to deformation (g) changing with increasing loading angles ($0 \leq \varphi \leq \pi/2 - \alpha$ and $n = 2$). (h) Poisson's ratio of the beam under compression. (i) The resistance changes introduced by the stretching of the hole wall or the microcracks within the pore wall.

3. Verification: piezoresistive behaviors of PPNs

3.1. Modal characteristics of OC cell

The FEA analysis using ABAQUS with a user-material subroutine (UMAT) subprogram (S7) aims to validate the predicted stress and sensitivity of intrinsic resistance of an OC model. The FEA model involves a beam with specific geometric ($L = 20\text{mm}$, $t = 2\text{mm}$, and $\alpha = 30^\circ$), mechanical properties ($E = 200\text{MPa}$ and $\mu = 0.49$), and electrical properties ($Xd_0 = 5\text{and} \rho = 10\Omega \cdot \text{mm}$). The loading conditions include symmetrical pressure in the vertical direction, constant current on the left side of the models, and constant temperature (potential) on the right side of the beam. To simulate bending models, free-moving edge bars are applied at the loading end. Moreover, a couple temperature-displacement module is utilized to analyze the resistance-deformation relationships in the model. To ensure the accuracy of FEA, the convergence (indicating the number of elements needed to ensure that the finite element analysis results are not affected by changes in the mesh size) is depicted in Figure S6. We define that the simulation results remain stable at or above 99.5 % convergence with the increase in the number of elements. The results indicate that approximately 30,000 C3D8T elements are employed to ensure sufficient convergence while dispersing the model. Fig. 5a illustrates the potential contours of the beam under bending deformation, while Figs. 5b and c show the dimensionless stress and sensitivity to deformation from the FEA and analytical models, indicating high consistency between them. This demonstrates the correctness of the theoretical model calculation. Based on this theoretical model, we have conducted a further analysis to investigate the impact of the following key parameters on the piezoresistive response.

Figs. 5d and e demonstrate the piezoresistive behaviors of different buckling modes ($1 \leq n$ and $\varphi = 0$), where stress and sensitivity to deformation increase with an increase in the buckling mode. Moreover, the piezoresistive sensitivity from buckling deformation at even inflection points is higher than that from odd inflection points. Previous SEM figures (Huang et al., 2022) also suggest that the buckling mode of order 2 is the most common in porous materials. As for the effect of different loading angles of the buckling deformation on piezoresistive behaviors, Figs. 5f and g show obvious yield characteristics, and the sensitivity to deformation reduces with increasing loading angles ($0 \leq \varphi \leq \pi/2 - \alpha$ and $n = 2$). In Fig. 5f, a discernible non-zero stress at the stretch ($\lambda=1$) is observed for the specific case of $\varphi=0$. This phenomenon is attributed to the axial pressure along the beam axis when $\varphi=0$, rendering the beam in a stable state. Consequently, there exists a yield stress causing non-zero stress at $\lambda=1$ for the case $\varphi=0$. In instances where the applied pressure is below the critical buckling yield stress of the beam, no buckling occurs, resulting in negligible displacement, as dictated by the large deflection formula (Eqs. (11) and 12). However, surpassing the critical buckling yield stress induces rapid buckling and a subsequent substantial increase in deformation. The dimensionless yield stress is about 0.08 %. Additionally, Poisson's ratio under compression is calculated in Fig. 5h, indicating that the bending mode of the beam exhibits a common Poisson's ratio effect, close to $-0.1 \sim -0.3$, which has been proven by many research studies (Kováčik, 2008; Zhang et al., 2024). However, the buckling mode shows a negative Poisson's ratio effect under large deformation, revealing the collapse of the hole wall causing the volume to shrink. To simplify the buckling model, the second-order buckling mode is used as the typical buckling deformation in follow-up studies. Due to complex deformations such as bending and different buckling deformations existing in a complex porous structure, hole walls can be stretched or misaligned to coordinate these complex deformation structures. Fig. 5i illustrates the resistance changes introduced by the stretching of the hole wall or the microcracks within the pore wall.

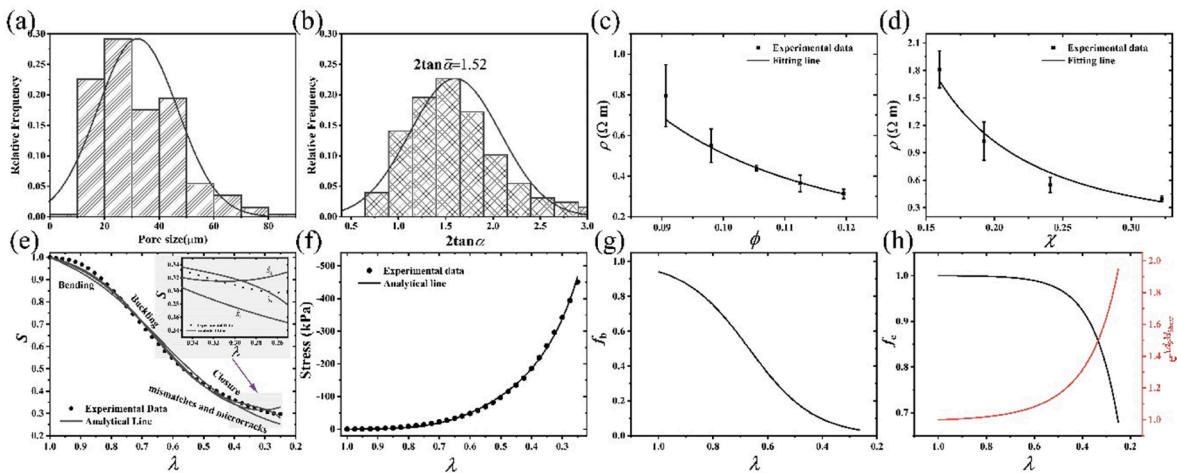


Fig. 6. Analytical and experimental piezoresistive behaviors of PFTN with a mass ratio of 7:3 between FKM and TPU. The pore distribution (a) and structure (height-width ratio) distribution (b) from image recognition software ImageJ. Resistivity changing different CB content (ϕ) (c) and relative density (χ) (d). (e) Three fitting functions considering different factors, such as only the over-transition from bending to buckling, the mismatch and microcracks, and finally the closure of the pores. (f) The fitting curves of stress considering the above three factors. (g) Boltzmann transition function from bending deformation to buckling deformation. (h) The exponential decay function describing the closure of pores and the resistance increase curve from mismatches and microcracks.

3.2. Quasi-static compression features of piezoresistive properties of PPN

To further verify the accuracy and practicability of the analytical model, PPNs are employed in experimental analysis. These PPNs are based on an inorganic salt pore-making process, with different elastomeric matrices (such as a typical linear polymer (TPU), a typical crosslink polymer (FKM), and their mixture) and different porosity. As an example, porous fluoroe elastomer- thermoplastic polyether urethanes nanocomposite (PFTN) with a mass ratio of 7:3 between FKM and TPU is used, and Figs. 6a and 6b show the pore distribution and structure (height-width ratio) distribution from image recognition software ImageJ. The average diameter distribution is close to the particle size of inorganic salts, and the aspect ratio indicates that the pore structure is nearly spheroid. To ensure uniform electrical conductivity across all directions, multiple measures are taken to control the physical properties of the material. Initially, nanoscale CB particles are utilized due to their excellent dispersibility and adsorption characteristics. Ultrasonic dispersion techniques and stabilizers are utilized to maximize the resistance of fine particles to Brownian motion, thereby minimizing the agglomeration of CB (Norisuye, 2017). Furthermore, inorganic salt pore-forming agents are employed. These agents undergo a rigorous grinding and sieving process to achieve particles with a targeted particle size distribution between 400 mesh and 500 mesh. The slurry viscosity is precisely controlled at a value exceeding 20,000 mPa·s. Based on the Stokes viscosity law, this precise control of viscosity minimizes the settling velocity of the dispersed phase particles, ensuring their uniform distribution within the slurry (Langlois et al., 2019). Finally, following the coating and drying of the sample, the sheet material undergoes a precision abrasive cutting process to remove the top and bottom surfaces. The resulting target sample has a thickness of approximately 1 mm, which approximately has isotropic electrical conductivity (Figure S8). Utilizing the aforementioned measures, target samples of PPNs with varying carbon nanoparticle content (ϕ) and relative density (χ) (S2) have been obtained. The sensitivity parameters (Xd_0 , sensitivity to deformation) of pore wall deformation have been rigorously established. Furthermore, the alterations in resistivity as a function of both carbon nanoparticle content and relative density are precisely depicted in Figs. 6c and d, respectively. Eq. (16) provides a fitting formula $\rho = 2.484 \times 10^{-5} e^{3.27\chi - 0.133\phi - 1/3} / \chi$, which can be used to obtain the value of $Xd_0 = 9.05$ when $\phi = 0.098$ and $\chi = 0.160$. Additionally, Eq. (1) yields $\eta = 0.166$ when $\chi = 0.160$. Using the adaptive moment estimation (ADAM) optimization algorithm (Xie et al., 2021), these free parameters can be optimized based on experimental data to obtain the optimal solution (S8). Fig. 6e shows three fitting functions that consider different factors, such as only the over-transition from bending to buckling ($\hat{S}_1 = f_b C_{bending} + (1 - f_b) C_{buckling}$), taking into account the microcracks ($\hat{S}_2 = [f_b C_{bending} + (1 - f_b) C_{buckling}] e^{X d_0 M_{shear}}$), and finally considering the closure of the pores ($\hat{S}_3 = f_c [f_b C_{bending} + (1 - f_b) C_{buckling}] e^{X d_0 M_{shear}}$). All three fitting functions have a fitting degree above 99.5%. When considering the closure of pores and micro-cracks, the piezoresistive curve can be better reduced. Based on the fitting function (\hat{S}_3), the fitting curves of stress are shown in Fig. 6f. The fitting degree (R^2) between the analytical model with parameters in Table 1 and the experimental results is more than 99%. Fig. 6g shows the Boltzmann transition function from bending deformation to buckling deformation with the transition center $\lambda_0 = 0.6673$. Fig. 6h shows the function f_c describing the closure of pores and the resistance increase curve $e^{X d_0 M_{shear}}$ from mismatches and microcracks. Both functions exhibit an exponential increase or decrease.

Fig. 7 shows the piezoresistive properties of PPN with different porosity (relative density) achieved by changing the usage of a pore-making agent (S2). Figs. 7a and 7b show the deformation sensitivity (Xd_0) of the pore wall and slenderness ratio (η) as they change with relative density. Increasing the relative density reduces the deformation sensitivity and increases the slenderness ratio. From these figures, it can be observed that when χ is equal to 0.137 and 0.192, Xd_0 is equal to 9.24 and 8.83, and η is equal to 0.153 and 0.183, respectively. Substituting these parameters into Eqs. (24) and 26 yields the fitting curves of stress and resistance sensitivity shown in Figs. 7c and 7d with fitting degrees above 99%. The free parameters can be obtained from Table 1. By comparing with the curves for $\chi = 0.160$, some patterns become evident. Increasing the relative density increases the stress, which is easy to understand due to the reduction of the effective medium for supporting forces. However, the resistance sensitivity decreases regardless of whether the relative density increases or decreases. The Boltzmann function (Fig. 7e) shows that the yield center also reduces with decreasing resistance sensitivity, indicating that PPN has the fastest transition from bending to buckling state, but increasing relative density may produce too much constraint, and decreasing relative density may be more suitable for bending mode generation. Fig. 7f depicts the pore closure behavior and the characteristics of microcrack propagation or mismatches in PPN with varying porosities under compressive conditions. The findings demonstrate that an increase in porosity results in an increase in sensitivity, but also leads to mismatched pore walls and increased occurrence of cracking. Therefore, PPN with $\chi=0.137$ exhibits lower piezoresistive sensitivity

Table 1
Key parameters of the analytical model describing the piezoresistive behaviors.

	Electrical model				Electrical and mechanical models		Mechanical model	
	χ	τ	A	ν	λ_0	w	c_1	c_2
PPN-1 (0.5 mm/min)	0.166	0.1038	3.5832	0.1733	0.6673	0.1193	0.7924	0.5518
PPN-1 (1.0 mm/min)	0.166	0.1362	3.1244	0.1480	0.6822	0.0830	0.8965	0.6460
PPN-1 (1.5 mm/min)	0.166	0.1311	3.0451	0.1179	0.7154	0.0843	0.9463	0.6864
PPN-1 (high ambient temperate)	0.166	0.1097	2.2514	0.1138	0.5696	0.0933	0.6945	0.3654
PPN-2	0.183	0.0687	8.4790	0.1424	0.5716	0.1257	0.6314	-0.1663
PPN-3	0.153	0.6361	1.1776	0.5429	0.6213	0.1247	0.2122	0.0335
PTN	0.2	0.0072	3.5789	0.2223	0.4680	0.2017	0.4778	-1.6613
PFN	0.176	0.0834	2.0255	0.3885	0.7352	0.1428	0.6470	0.1864

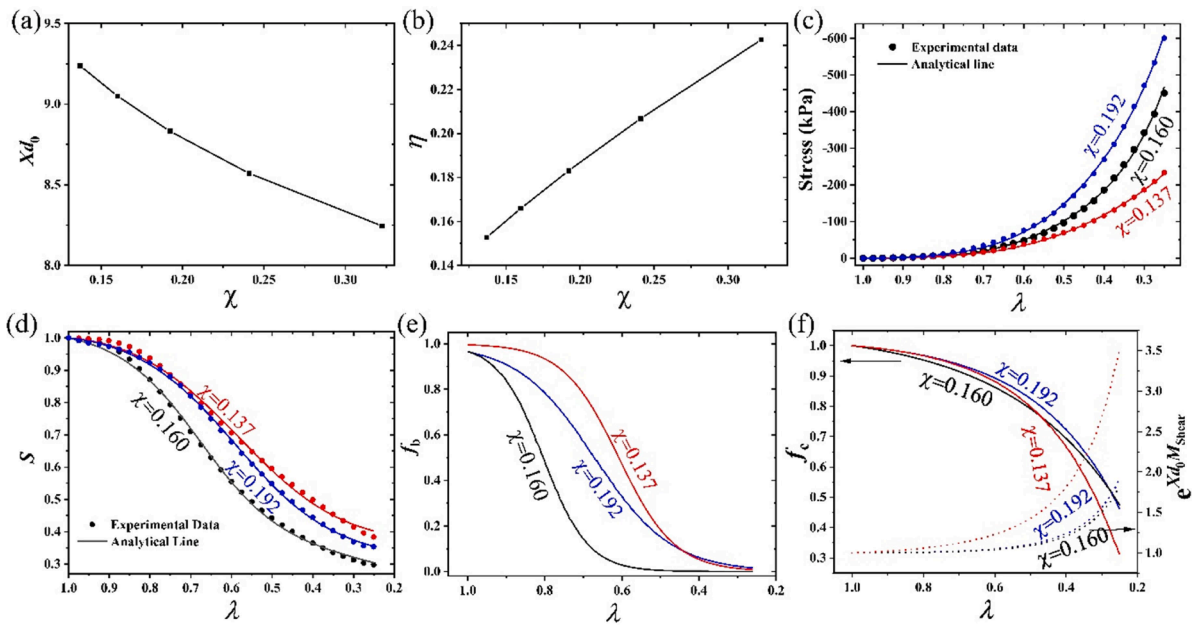


Fig. 7. Piezoresistive properties of PPN with different porosity (relative density) achieved by changing the usage of the pore-making agent. The deformation sensitivity (X_{d0}) (a) and slenderness ratio (η) (b) changing with relative density. The experimental and fitting curves of stress (c) and resistance sensitivity (d) changing with relative density. (e) The Boltzmann function transiting from bending to buckling state. (f) The exponential decay function describing the closure of pore and the resistance increase curve changing with relative density.

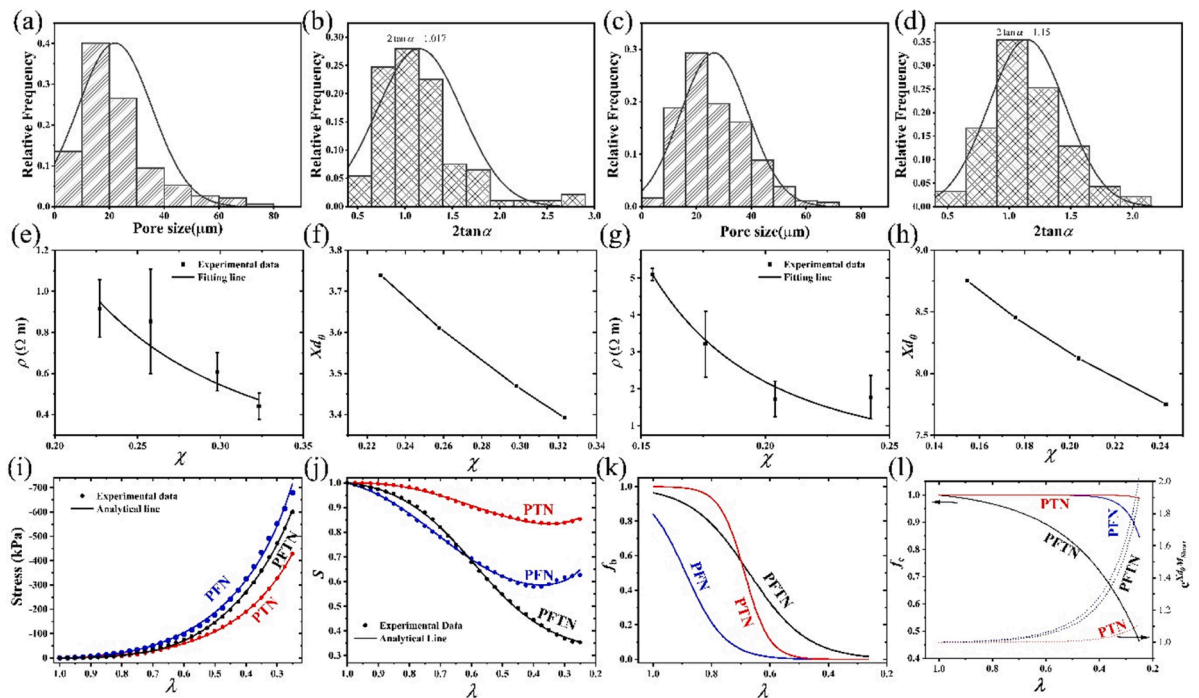


Fig. 8. Piezoresistive response characteristics of PPN utilizing different elastomeric matrices (TPU and FKM). Aperture distribution (a, c) and aperture aspect ratio distribution (b, d) of PTN and PFN, respectively. The changing curves of resistivity of PTN (e) and PFN (g) along with relative density. The deformation sensitivity of PTN (f) and PFN (h) changing with relative density. The matching stress curves (i) and resistance sensitivity curves (j) of PFTN (black line), PTN (red line), and PFN (blue line) between the analytical model and experimental data. (k) The Boltzmann function transiting from bending to buckling state of PFTN (black line), PTN (red line), and PFN (blue line). (l) The exponential decay function describing the closure of pore and the resistance increase curves of PFTN (black line), PTN (red line), and PFN (blue line).

because of its higher porosity.

In this section, the piezoresistive response characteristics of PPN utilizing different elastomeric matrices (TPU and FKM) are compared. Figs. 8a, b, c, and d show the aperture distribution and aperture aspect ratio distribution of these PPNs. The mean of the aperture aspect ratio of these PPNs can be obtained as follows: $\tan\bar{\alpha}_{PTN} = 0.5085$ and $\tan\bar{\alpha}_{PFN} = 0.575$. According to the changing curves of resistivity of porous thermoplastic polyether urethanes nanocomposite (PTN) and porous fluoroelastomer nanocomposite (PFN) along with relative density in Figs. 8e and 8g, equations describing resistivity changing with deformation can be obtained as $\rho = 2.13 \times 10^{-4} e^{2.513\chi^{-0.146}\phi^{-1/3}} / \chi$ and $\rho = 1.94 \times 10^{-5} e^{3.45\chi^{-0.22}\phi^{-1/3}} / \chi$ for PTN with $\phi=0.0916$ and PFN with $\phi=0.1185$, respectively. Figs. 8f and 8h show the deformation sensitivity changing with relative density. Thus, we can obtain $Xd_0=2.28$ for PTN with $\chi=0.227$ (yields $\eta=0.2$), which is fabricated by 6.5 times usage of pore-making agent and 0.15wt% CB against the matrix, and $Xd_0=5.70$ for PFN with $\chi=0.176$ (yields $\eta=0.176$), which is fabricated by 6 times usage of pore-making agent and 0.13wt% CB against the matrix. Substituting these parameters into Eqs. (25) and 27, Figs. 8i and 8j show the matching stress curves and resistance sensitivity curves between the analytical model and experimental data. Different from the piezoresistive behaviors of PFTN, a noticeable rise in resistance occurred in the second half of the compression. Figs. 8k and 8l, combined with SEM figures of PTN and PFN (S9), explain this difference in detail. The smooth and complete pore wall structure of PTN makes it more elastic and less prone to yield, and the decrease in resistance from the closure of pores is less than the increase from mismatches and microcracks. Due to the micropore within PFN, buckling is more likely to occur (blue line in Fig. 8k), and mismatches and microcracks are more likely to occur, increasing resistance (blue dot in Fig. 8l). The mixed matrix benefits from the microstructure within the pore wall from FKM, which increases the piezoresistive sensitivity, while the supporting effect of TPU enhances the ability to resist yielding and breaking (S9).

3.3. Quasi-static cyclic compression feature of PPN

The preceding studies have demonstrated the analytical model's capacity to describe the piezoresistive behaviors of PPN and explain the complex piezoresistive phenomenon depicted in Figs. 1c, d, and e, which is the combined effect of bending beam, buckling beam, pore closure, and mismatches and microcracks within the pore wall. Nevertheless, the apparent resistance overshooting is observed upon releasing the compressed PPE in Figs. 1f and g necessitate further analysis. Due to the relaxation effect of the polymer matrix, the recovery of the transition from buckling to bending, the opening of closed pores, and the restoration of mismatches and microcracks do not precisely coincide with the original function. To model the experimental piezoresistive phenomenon, we employed the following equations to describe the recovery of the transition from buckling to bending, the opening of closed pores, and the restoration of mismatches and microcracks,

$$\begin{cases} \tilde{f}_b = 1 - (1 + e^{(\lambda-\lambda_0)/\tilde{w}})^{-1} \\ \tilde{f}_c = 1 - [1 - f_c(0.25)] / (1 + e^{(\lambda-\lambda_c)/\tilde{w}_c})^{-1} \\ \Delta\tilde{\mu} = \Delta\mu(0.25) + \left(e^{\frac{-\lambda}{\tilde{\tau}}} - e^{\frac{-0.25}{\tilde{\tau}}} \right) / \left(2 - 2e^{\frac{-1}{\tilde{\tau}}} \right) \end{cases} \quad (28)$$

By substituting the above functions into Eqs. (25) and 27, the recovery curves of the dimensionless stress and piezoresistive sensitivity can be obtained as shown in Figs. 9a and b. The free parameters for these functions are presented in Table 2, using the PFTN sample with $\chi=0.160$. The stress curve exhibits significant hysteresis, where the recovery stress is lower than the loading stress. This hysteresis can be attributed to pore collapse and creep of the elastic matrix, leading to faster stress recovery. The steeper transition curve from buckling deformation to bending deformation during the recovery process compared to the loading process, as shown in Fig. 9c, is due to the higher buckling stress decreasing to the bending stress more rapidly. Regarding the resistance hysteresis, the recovery resistance is greater than the loading resistance. According to the analytical model, mismatches and microcracks are the primary reasons for increasing resistance during compression. Therefore, the high resistance overshooting (where the recovery resistance is 1.4 times the original resistance upon releasing the PFTN) is mainly due to the slow deformation recovery of mismatches within pore walls and/or permanent deformation of microcracks within the pore wall (as illustrated in Fig. 9d). This also explains why

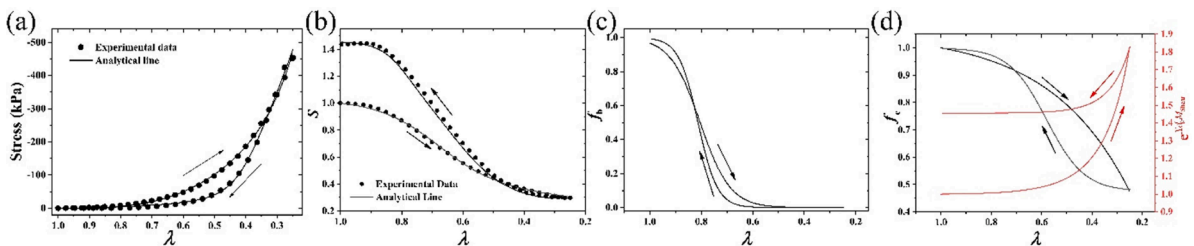


Fig. 9. Cyclic piezoresistive characteristics of the PFTN with a mass ratio of 7:3 between FKM and TPU. The cyclic characteristics curves of dimensionless stress curve (a) and piezoresistive sensitivity curve (b). (c) Cyclic transition curves between bending deformation and buckling deformation. (d) The cyclic characteristics of the exponential decay function describing the closure of pores and the resistance increase curves from mismatches and microcracks within pore walls.

many porous PPEs have a low first piezoresistive sensitivity, as observed in Figs. 1d and f.

In addition, loading speeds and ambient temperature, which are two key factors that determine the piezoresistive response, were also studied. Previous research (Madhuri et al., 2020; Zhai et al., 2015; Zheng et al., 2004) on the relaxation and creep behaviors of elastomers has revealed that faster loading speeds result in a higher stress response due to the higher mechanical resistance from the hysteresis of deformation. In contrast, a higher ambient temperature leads to a decrease in stress response due to the softening effect at higher temperatures. Fig. 10a shows a similar stress response of PPN to that of an elastomer, with steeper recovery transition curves (as shown in Fig. 10c). Furthermore, faster loading speeds and higher temperatures are beneficial in reducing the hysteresis due to smaller creep deformation. Fig. 10b exhibits the piezoresistive response of the PFTN under different loading speeds and ambient temperatures. The most noticeable feature is that the resistance overshooting is lower under faster loading speeds and higher ambient temperatures. This can be explained by the faster opening of closed pores (as shown in Fig. 10d) and smaller mismatches and microcracks (as shown in Fig. 10e) resulting from smaller creep deformation under compression.

Fig. 11 illustrates the piezoresistive behaviors of PPN with different relative densities and elastic matrices. The stress response (as shown in Fig. 11a) reduces with an increase in porosity, which can be easily understood due to the reduction of material effectively resistant to deformation (Stoia et al., 2019). However, the resistance response (as shown in Fig. 11b) displays high resistance overshooting of the PFTN with $\chi=0.160$. By increasing porosity, a clear pattern can be observed from the transition curve (as shown in Fig. 11e), closure and opening of the pore (as shown in Fig. 11f), and changing curves of mismatch and microcracks (as shown in Fig. 11g), indicating faster transition recovery, faster opening of closed pores, and larger mismatch and microcracks are generated. However, there are some nonconformities such as higher pore closure of the PFTN with $\chi=0.160$ in the middle of Fig. 11f. This is mainly due to the collapsed pores of PPE during the molding process. Therefore, although PFTN with $\chi=0.137$ has a smaller relative density, smaller pore closure reduces the piezoresistive sensitivity. Furthermore, Figs. 11c and d exhibit stress recovery and resistance recovery of PTN and PFN, respectively. PTN with a high resilience matrix (TPU) shows faster transition recovery (as shown in Fig. 11h), smaller pore closure (as shown in Fig. 11i), and smaller mismatch and microcracks (as shown in Fig. 11j), resulting in a lower piezoresistive sensitivity compared with similar PFTN with $\chi=0.192$. However, there are more micropores within the pore walls of PFN than PFTN, slower transition recovery (as shown in Fig. 11h), smaller pore closure (as shown in Fig. 11i), and larger mismatch and microcracks (as shown in Fig. 11j) cause a larger resistance hysteresis loop (as shown in Fig. 11d) due to the lack of supporting effect of high resilience matrix (TPU).

4. Conclusion

In this paper, an analytical model for PPE has been proposed to reveal the mechanisms of piezoresistive behaviors, including bidirectional piezoresistive trends and resistance overshooting. Bending and buckling cell ligaments, closure or opening of pores, and mismatch and microcrack within pore wall affect the conductive networks within compressed PPEs. The good agreement between the experimental results and analytical results demonstrates the analytical model has a high potential for the design of PPN with excellent piezoresistive properties. One of the significant conclusions is that mismatch and microcracks within the pore wall generated by the collapse of pores from excessive compressive deformation are the fundamental causes of the bidirectional piezoresistive phenomenon. Suitable matrix material composition (such as a mixture of TPU and FKM) can effectively generate uniform pore structures to reduce the mismatches and cracks within the pore wall. Increasing porosity increases the closure of pores, which is beneficial to increase the piezoresistive sensitivity. The formation mechanism of high resistance overshooting can be explained by that the recovery of mismatch and microcrack along with segmental movement increasing resistance is slower than that of bending and buckling deformation from the configurational change of the molecular chains, which reduces the resistance. Increasing loading speed and ambient temperature can reduce the creep deformation under compression, hence decreasing the overshooting of the resistance. From a broader perspective, this study highlights the rational micro/nano structural design with various PPN materials to achieve excellent piezoresistive responses. Due to the longer creep and relaxation period of elastomer than other solid matrices, the recovery of overshooting resistance of the sensor made by PFTN is longer than traditional piezoresistive sensor.

Table 2
Key parameters of the analytical model describing the recovery of piezoresistive behaviors.

	χ	Electrical model			Electrical and mechanical models		Mechanical model	
		$\tilde{\lambda}_c$	\tilde{w}_c	$\tilde{\tau}$	$\tilde{\lambda}_0$	\tilde{w}	\tilde{c}_1	\tilde{c}_2
PPN-1 (0.5 mm/min)	0.166	0.3822	0.0780	0.1086	0.6874	0.0890	1.6290	1.5555
PPN-1 (1.0 mm/min)	0.166	0.3803	0.0588	0.1064	0.6352	0.0803	1.3791	1.2543
PPN-1 (1.5 mm/min)	0.166	0.3478	0.0480	0.0892	0.6151	0.0771	1.3164	1.1658
PPN-1 (high ambient temperate)	0.166	0.3112	0.0298	0.0925	0.4816	0.0759	0.8108	0.5196
PPN-2	0.183	0.2651	0.0504	0.1056	0.5814	0.0981	1.1075	0.7756
PPN-3	0.153	0.6613	0.1013	0.3712	0.4293	0.0700	0.4240	0.2953
PTN	0.2	0.2651	0.0504	0.1993	0.4389	0.1829	0.6633	0.4507
PFN	0.176	0.7826	0.0394	0.3232	0.5337	0.1018	1.1135	0.9342

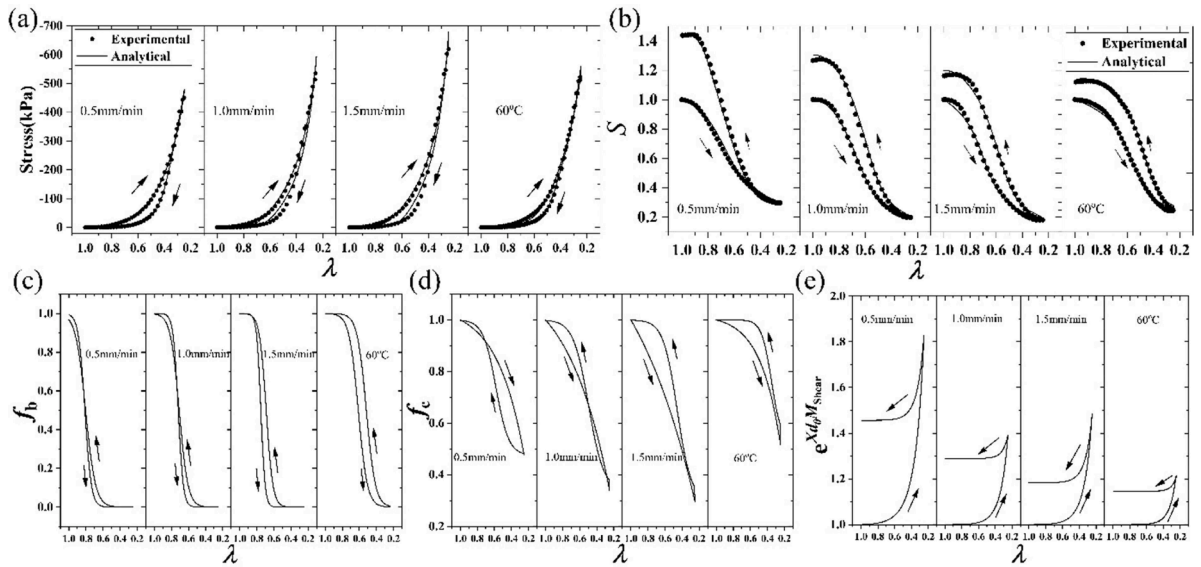


Fig. 10. Cyclic piezoresistive characteristics of the PFTN under different loading speeds and ambient temperatures. Cyclic stress response (a) and resistance response (b) of the PFTN. Cyclic transition curves between bending deformation and buckling deformation (c), cyclic characteristics of the closure of pore(d), and cyclic exponential growth function from mismatches and microcracks within pore walls (e) under different loading conditions.

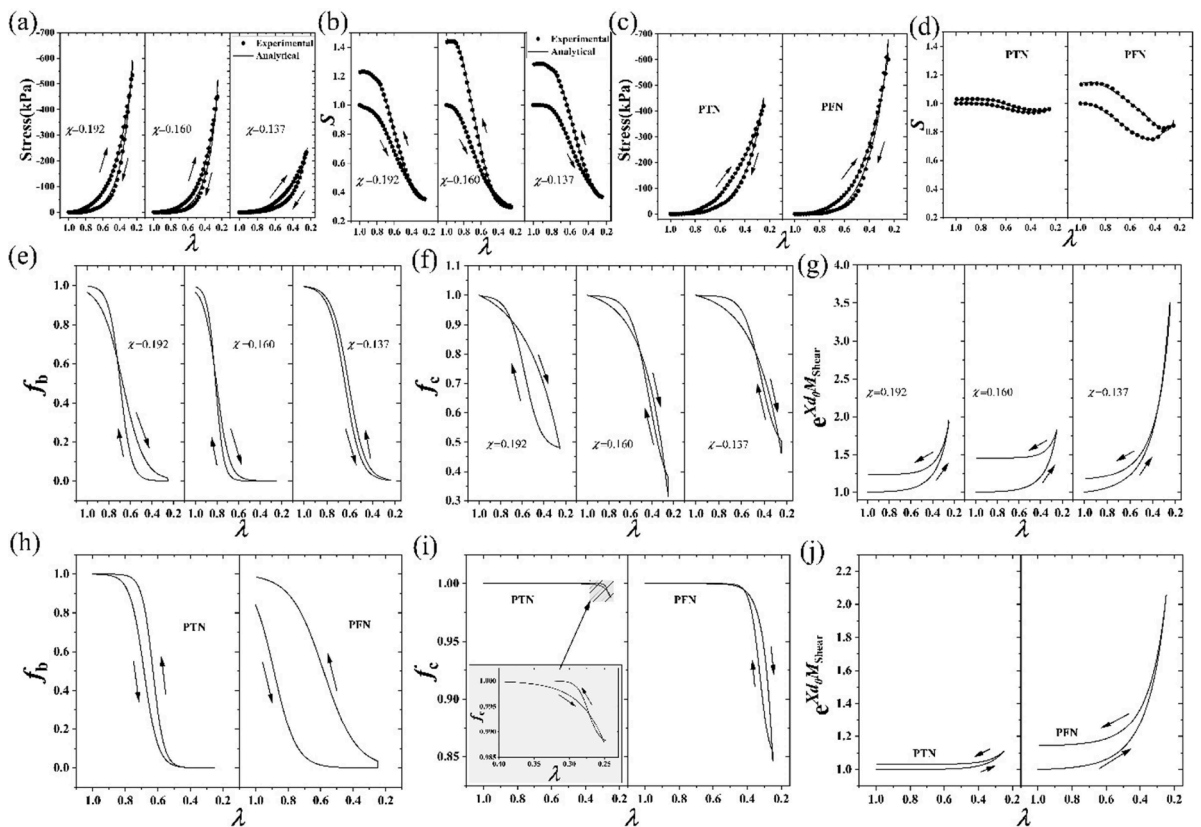


Fig. 11. The cyclic piezoresistive behaviors of PPNs with different relative densities and elastic matrices. The stress response (a, c) and the resistance response (b, d) of PPNs with different relative densities and elastic matrices. The transition curve (e, h), closure and opening of the pore (f, i), and changing curves of mismatch and microcracks (g, j) of PPNs with different relative densities and elastic matrices, respectively.

CRedit authorship contribution statement

Jianpeng Zhang: Conceptualization, Data curation, Formal analysis, Investigation, Methodology, Validation, Visualization, Writing – original draft. **Song Wei:** Methodology, Formal analysis, Data curation. **Chao Shang:** Visualization, Software, Methodology, Formal analysis. **Yu Duan:** Software, Investigation, Formal analysis, Data curation. **Zhaoqiang He:** Investigation, Formal analysis, Data curation. **Hua An:** Writing – review & editing, Visualization, Validation, Methodology, Investigation, Funding acquisition. **Xinge Yu:** Writing – review & editing, Visualization, Validation, Methodology. **Zhengchun Peng:** Conceptualization, Funding acquisition, Project administration, Resources, Software, Supervision, Writing – review & editing.

Declaration of competing interest

The authors declare that they have no known competing financial interests or personal relationships that could have appeared to influence the work reported in this paper.

Data availability

Data will be made available on request.

Acknowledgments

This work was financially supported in part by the joint funding program of Guangdong Department of Science and Technology and Hongkong Innovation and Technology Fund under grant 2021A0505110015, and the Science and Technology Innovation Council of Shenzhen under grants KQTD20170810105439418 and JCYJ20200109114237902, and National Natural Science Foundation of China under grant 22005198.

Supplementary materials

Supplementary material associated with this article can be found, in the online version, at [doi:10.1016/j.ijengsci.2024.104091](https://doi.org/10.1016/j.ijengsci.2024.104091).

Appendix A. Derivation of Eq. (11) for beam length constraint condition and displacement constraint condition

When n is an even number, the buckling mode exhibits a symmetric buckling mode. Thus, the length of the beam can be written as,

$$\begin{aligned}
 L &= \sqrt{\frac{EI}{2F_r}} \sum_{i=1}^{2n} \int_{\theta^* \sin\left(\frac{i+1}{2}\pi\right)}^{\theta^* \sin\left(\frac{i+2}{2}\pi\right)} \frac{\left(\sin\left(\frac{i-1}{2}\pi\right) - \sin\left(\frac{i}{2}\pi\right)\right)}{\sqrt{\frac{2F_r}{EI} \sqrt{\cos(\varphi - \theta) - \cos(\varphi + \theta^*)}}} d\theta \\
 &= 2n \sqrt{\frac{EI}{2F_r}} \int_0^{\theta^*} \frac{1}{\sqrt{\frac{2F_r}{EI} \sqrt{\cos(\varphi - \theta) - \cos(\varphi + \theta^*)}}} d\theta
 \end{aligned}
 \tag{A.1}$$

Thus, the displacement of the beam end can be written as

$$x_m = 2n \sqrt{\frac{EI}{2F_r}} \int_0^{\theta^*} \frac{\cos\theta}{\sqrt{\frac{2F_r}{EI} \sqrt{\cos(\varphi - \theta) - \cos(\varphi + \theta^*)}}} d\theta,
 \tag{A.2}$$

$$\begin{aligned}
 y_m &= \sqrt{\frac{EI}{2F_r}} \sum_{i=1}^{2n} \int_{\theta^* \sin\left(\frac{i+1}{2}\pi\right)}^{\theta^* \sin\left(\frac{i+2}{2}\pi\right)} \frac{\left(\sin\left(\frac{i-1}{2}\pi\right) - \sin\left(\frac{i}{2}\pi\right)\right) \cos\theta}{\sqrt{\frac{2F_r}{EI} \sqrt{\cos(\varphi - \theta) - \cos(\varphi + \theta^*)}}} d\theta \\
 &= n \sqrt{\frac{EI}{2F_r}} \int_0^{\theta^*} \frac{\sin(\theta)}{\sqrt{\frac{2F_r}{EI} \sqrt{\cos(\varphi - \theta) - \cos(\varphi + \theta^*)}}} d\theta \\
 &\quad - n \sqrt{\frac{EI}{2F_r}} \int_{-\theta^*}^0 \frac{-\sin(\theta)}{\sqrt{\frac{2F_r}{EI} \sqrt{\cos(\varphi - \theta) - \cos(\varphi + \theta^*)}}} d\theta \\
 &= 0
 \end{aligned}
 \tag{A.3}$$

When n is an odd number, the buckling mode exhibits an asymmetric buckling mode.

$$\begin{aligned}
 L &= \sqrt{\frac{EI}{2F_r}} \sum_{i=1}^{2n} \int_{\theta^* \sin\left(\frac{i+1}{2}\pi\right)}^{\theta^* \sin\left(\frac{i+2}{2}\pi\right)} \frac{\left(\sin\left(\frac{i-1}{2}\pi\right) - \sin\left(\frac{i}{2}\pi\right)\right)}{\sqrt{\frac{2F_r}{EI} \sqrt{\cos(\varphi - \theta) - \cos(\varphi + \theta^*)}}} d\theta \\
 &= (n+1) \sqrt{\frac{EI}{2F_r}} \int_0^{\theta^*} \frac{1}{\sqrt{\frac{2F_r}{EI} \sqrt{\cos(\varphi - \theta) - \cos(\varphi + \theta^*)}}} d\theta \\
 &\quad - (n-1) \sqrt{\frac{EI}{2F_r}} \int_{-\theta^*}^0 \frac{-1}{\sqrt{\frac{2F_r}{EI} \sqrt{\cos(\varphi - \theta) - \cos(\varphi + \theta^*)}}} d\theta \\
 &= 2n \sqrt{\frac{EI}{2F_r}} \int_0^{\theta^*} \frac{1}{\sqrt{\frac{2F_r}{EI} \sqrt{\cos(\varphi - \theta) - \cos(\varphi + \theta^*)}}} d\theta
 \end{aligned} \tag{A.4}$$

Thus, the displacement of the beam end can be written as

$$x_m = 2n \sqrt{\frac{EI}{2F_r}} \int_0^{\theta^*} \frac{\cos(\theta)}{\sqrt{\frac{2F_r}{EI} \sqrt{\cos(\varphi - \theta) - \cos(\varphi + \theta^*)}}} d\theta, \tag{A.5}$$

$$\begin{aligned}
 y_m &= \sqrt{\frac{EI}{2F_r}} \sum_{i=1}^{2n} \int_{\theta^* \sin\left(\frac{i+1}{2}\pi\right)}^{\theta^* \sin\left(\frac{i+2}{2}\pi\right)} \frac{\left(\sin\left(\frac{i-1}{2}\pi\right) - \sin\left(\frac{i}{2}\pi\right)\right) \sin\theta}{\sqrt{\frac{2F_r}{EI} \sqrt{\cos(\varphi - \theta) - \cos(\varphi + \theta^*)}}} d\theta \\
 &= (n+1) \sqrt{\frac{EI}{2F_r}} \int_0^{\theta^*} \frac{\sin(\theta)}{\sqrt{\frac{2F_r}{EI} \sqrt{\cos(\varphi - \theta) - \cos(\varphi + \theta^*)}}} d\theta \\
 &\quad - (n-1) \sqrt{\frac{EI}{2F_r}} \int_{-\theta^*}^0 \frac{-\sin(\theta)}{\sqrt{\frac{2F_r}{EI} \sqrt{\cos(\varphi - \theta) - \cos(\varphi + \theta^*)}}} d\theta \\
 &= 2 \sqrt{\frac{EI}{2F_r}} \int_0^{\theta^*} \frac{\sin(\theta)}{\sqrt{\frac{2F_r}{EI} \sqrt{\cos(\varphi - \theta) - \cos(\varphi + \theta^*)}}} d\theta
 \end{aligned} \tag{A.6}$$

To sum up, the displacement constraints of the beam end and the beam length constraints can be summarized as

$$\left\{ \begin{aligned}
 L &= 2n \int_0^{\theta^*} \frac{1}{\sqrt{\frac{2F_r}{EI} \sqrt{\cos(\varphi - \theta) - \cos(\varphi + \theta^*)}}} d\theta \\
 x_m &= 2n \int_0^{\theta^*} \frac{\cos(\theta)}{\sqrt{\frac{2F_r}{EI} \sqrt{\cos(\varphi - \theta) - \cos(\varphi + \theta^*)}}} d\theta \\
 y_m &= [1 - (-1)^n] \int_0^{\theta^*} \frac{\sin(\theta)}{\sqrt{\frac{2F_r}{EI} \sqrt{\cos(\varphi - \theta) - \cos(\varphi + \theta^*)}}} d\theta
 \end{aligned} \right. \tag{A.7}$$

References

Arh, M., Slavič, J., & Boltežar, M. (2021). Design principles for a single-process 3d-printed accelerometer – theory and experiment. *Mechanical Systems and Signal Processing*, 152, Article 107475.

Ashby, M. F., & Medalist, R. F. M. (1983). The mechanical properties of cellular solids. *Metallurgical Transactions A*, 14, 1755–1769.

Avalle, M., Belingardi, G., & Ibba, A. (2007). Mechanical models of cellular solids: Parameters identification from experimental tests. *International Journal of Impact Engineering*, 34, 3–27.

- Chen, Y., & Jin, L. (2021). Reusable energy-absorbing architected materials harnessing snapping-back buckling of wide hyperelastic columns. *Advanced Functional Materials*, *31*, Article 2102113.
- Chen, Y., Das, R., & Battley, M. (2017). Finite element analysis of the compressive and shear responses of structural foams using computed tomography. *Composite Structures*, *159*, 784–799.
- Cousins, R. R. (1976). A theory for the impact behavior of rate-dependent padding materials. *Journal of Applied Polymer Science*, *20*, 2893–2903.
- Ezquerro, T. A., Kuleszka, M., Cruz, C. S., & Baltá-Calleja, F. J. (1990). Charge transport in polyethylene-graphite composite materials. *Advanced Materials*, *2*, 597–600.
- Fu, R., Zhao, X., Zhang, X., & Su, Z. (2023). Design strategies and applications of wearable piezoresistive strain sensors with dimensionality-based conductive network structures. *Chemical Engineering Journal*, *454*, Article 140467.
- Goga, V. (2011). New phenomenological model for solid foams. In J. Murín, V. Komiš, & V. Kutíš (Eds.), *Computational modelling and advanced simulations* (pp. 67–82). Dordrecht: Springer Netherlands.
- Grossi, B., Palza, H., Zagal, J. C., Falcón, C., & During, G. (2021). Metarpillar: Soft robotic locomotion based on buckling-driven elastomeric metamaterials. *Materials & Design*, *212*, Article 110285.
- Gu, Y., Xu, Z., Fan, F., Wei, L., Wu, T., & Li, Q. (2023a). Highly breathable, stretchable, and tailorable tpu foam for flexible gas sensors. *ACS Sensors*, *8*, 3772–3780.
- Gu, X., Li, X., Xia, X., Madenci, E., & Zhang, Q. (2023b). A robust peridynamic computational framework for predicting mechanical properties of porous quasi-brittle materials. *Composite Structures*, *303*, Article 116245.
- Han, T., Yan, H., Xu, D., & Fu, L.-Y. (2020). Theoretical correlations between the elastic and electrical properties in layered porous rocks with cracks of varying orientations. *Earth-Science Reviews*, *211*, Article 103420.
- Huang, C., Bian, Z., Fang, C., Zhou, X., & Song, J. (2018). Experimental and theoretical study on mechanical properties of porous PDMS. *Journal of Applied Mechanics*, *85*, 041009.
- Huang, X., Guo, W., Liu, S., Li, Y., Qiu, Y., Fang, H., et al. (2022). Flexible mechanical metamaterials enabled electronic skin for real-time detection of unstable grasping in robotic manipulation. *Advanced Functional Materials*, *32*, Article 2109109.
- Ji, F., Sun, Z., Hang, T., Zheng, J., Li, X., Duan, G., et al. (2022). Flexible piezoresistive pressure sensors based on nanocellulose aerogels for human motion monitoring. *Composites Communications*, *35*, Article 101351.
- Jo, C., & Naguib, H. E. (2007). Constitutive modeling of HDPE polymer/clay nanocomposite foams. *Polymer*, *48*, 3349–3360.
- Kaiser, A. (2000). Electronic transport properties of conducting polymers and carbon nanotubes. *Reports on Progress in Physics*, *64*, 1.
- Kováčik, J. (2008). Correlation between elastic modulus, shear modulus, Poisson's ratio and porosity in porous materials. *Advanced Engineering Materials*, *10*, 250–252.
- Langlois, V., Trinh, V. H., & Perrot, C. (2019). Electrical conductivity and tortuosity of solid foam: Effect of pore connections. *Physical Review E*, *100*, Article 013115.
- Li, X., Liu, Z., Cui, S., Luo, C., Li, C., & Zhuang, Z. (2019). Predicting the effective mechanical property of heterogeneous materials by image based modeling and deep learning. *Computer Methods in Applied Mechanics and Engineering*, *347*, 735–753.
- Li, W., Jin, X., Han, X., Li, Y., Wang, W., Lin, T., et al. (2021a). Synergy of porous structure and microstructure in piezoresistive material for high-performance and flexible pressure sensors. *ACS Applied Materials & Interfaces*, *13*, 19211–19220.
- Li, X., Li, X., Liu, T., Lu, Y., Shang, C., Ding, X., et al. (2021b). Wearable, washable, and highly sensitive piezoresistive pressure sensor based on a 3d sponge network for real-time monitoring human body activities. *ACS Applied Materials & Interfaces*, *13*, 46848–46857.
- Liu, Q., & Subhash, G. (2004). A phenomenological constitutive model for foams under large deformations. *Polymer Engineering & Science*, *44*, 463–473.
- Liu, Y., Liang, T., Fu, Y., Xie, Y.-X., & Wang, Y.-S. (2022). A novel buckling pattern in periodically porous elastomers with applications to elastic wave regulations. *Extreme Mechanics Letters*, *54*, Article 101781.
- Liu, P. S. (2010). Mechanical relation for porous metal foams under complex loads of triaxial tension and compression. *Materials & Design*, *31*, 2264–2269.
- Luo, G., Zhu, Y., Zhang, R., Cao, P., Liu, Q., Zhang, J., et al. (2021). A review on mechanical models for cellular media: investigation on material characterization and numerical simulation. *Polymers*, *13*, 3283.
- Lv, Y., Wang, B., Liu, G., Tang, Y., Lu, E., Xie, K., et al. (2021). Metal material, properties and design methods of porous biomedical scaffolds for additive manufacturing: A review. *Frontiers in Bioengineering and Biotechnology*, *9*.
- Lv, C., Tian, C., Jiang, J., Dang, Y., Liu, Y., Duan, X., et al. (2023). Ultrasensitive linear capacitive pressure sensor with wrinkled microstructures for tactile perception. *Advanced Science*, *10*, Article 2206807.
- Ma, L. Y., Zhao, Y., Yu, Z., Zhang, Z. X., & Wen, S. (2022). Development of fluororubber foam by supercritical N₂ foaming through irradiation pre-crosslinking and secondary cross-linking. *Polymers for Advanced Technologies*, *33*, 3437–3446.
- Madhuri, S. N., Murugendrapa, M. V., & Rukmani, K. (2020). Conduction and relaxation mechanisms in gadolinium oxide nanoparticle doped polyvinyl alcohol films. *Materials Today Communications*, *23*, Article 100942.
- Meena, K. V., & Sankar, A. R. (2021). Biomedical catheters with integrated miniature piezoresistive pressure sensors: A review. *IEEE Sensors Journal*, *21*, 10241–10290.
- Nan, Z., Wei, W., Lin, Z., Chang, J., & Hao, Y. (2023). Flexible nanocomposite conductors for electromagnetic interference shielding. *Nano-Micro Letters*, *15*, 172.
- Norisuye, T. (2017). Structures and dynamics of microparticles in suspension studied using ultrasound scattering techniques. *Polymer International*, *66*, 175–186.
- Notaros, B. M. (2011). *Electromagnetics*. NJ: Prentice Hall Upper Saddle River.
- Prabagar, C. J., Anand, S., Vu, M. C., Tran, M.-S., Mani, D., Martina, M. M., et al. (2023). Thermally insulating carbon nanotubes and copper ferrite based porous polydimethylsiloxane foams for absorption-dominant electromagnetic interference shielding performance. *Composites Communications*, *42*, Article 101691.
- Rahman, O., Uddin, K. Z., Muthulingam, J., Youssef, G., Shen, C., & Koohbor, B. (2022). Density-graded cellular solids: mechanics, fabrication, and applications. *Advanced Engineering Materials*, *24*, Article 2100646.
- Rong, Q., Wei, H., Huang, X., & Bao, H. (2019). Predicting the effective thermal conductivity of composites from cross sections images using deep learning methods. *Composites Science and Technology*, *184*, Article 107861.
- Rusch, K. C. (1970). Energy-absorbing characteristics of foamed polymers. *Journal of Applied Polymer Science*, *14*, 1433–1447.
- Schlumberger, C., & Thommes, M. (2021). Characterization of hierarchically ordered porous materials by physisorption and mercury porosimetry—A tutorial review. *Advanced Materials Interfaces*, *8*, Article 2002181.
- Sherwood, J. A., & Frost, C. C. (1992). Constitutive modeling and simulation of energy absorbing polyurethane foam under impact loading. *Polymer Engineering & Science*, *32*, 1138–1146.
- Shi, X., Zhu, Y., Fan, X., Wu, H.-A., Wu, P., Ji, X., et al. (2022). An auxetic cellular structure as a universal design for enhanced piezoresistive sensitivity. *Matter*, *5*, 1547–1562.
- Shrimali, B., Parnell, W. J., & Lopez-Pamies, O. (2020). A simple explicit model constructed from a homogenization solution for the large-strain mechanical response of elastomeric syntactic foams. *International Journal of Non-Linear Mechanics*, *126*, Article 103548.
- Sohrab, S. H. (2022). Universality of Boltzmann statistical mechanics, thermodynamics, quantum mechanics, and Shannon information theory. In C. H. Skiadas, & Y. Dimotikalis (Eds.), *14th Chaotic Modeling and Simulation International Conference* (pp. 445–480). Cham: Springer International Publishing.
- Stoia, D. I., Linul, E., & Marsavina, L. (2019). Influence of manufacturing parameters on mechanical properties of porous materials by selective laser sintering. *Materials*, *12*, 871.
- Storåkers, B. (1986). On material representation and constitutive branching in finite compressible elasticity. *Journal of the Mechanics and Physics of Solids*, *34*, 125–145.
- Su, Y., Zhu, J., Long, X., Zhao, L., Chen, C., & Liu, C. (2023). Statistical effects of pore features on mechanical properties and fracture behaviors of heterogeneous random porous materials by phase-field modeling. *International Journal of Solids and Structures*, *264*, Article 112098.
- Vimala, A., & Vandrangi, S. K. (2023). Development of porous materials based resistance pressure sensors and their biomedical applications: A review. *International Journal of Polymeric Materials and Polymeric Biomaterials*, *72*, 1558–1577.

- Wang, Y., Chen, Z., Lu, Y., Yang, L., Xu, T., Wu, H., et al. (2023). A review of application, modification, and prospect of melamine foam. *Nanotechnology Reviews*, 12, Article 20230137.
- Wu, X., Han, Y., Zhang, X., Zhou, Z., & Lu, C. (2016). Large-area compliant, low-cost, and versatile pressure-sensing platform based on microcrack-designed carbon Black@Polyurethane sponge for human-machine interfacing. *Advanced Functional Materials*, 26, 6246–6256.
- Xie, Q., Suvama, M., Li, J., Zhu, X., Cai, J., & Wang, X. (2021). Online prediction of mechanical properties of hot rolled steel plate using machine learning. *Materials & Design*, 197, Article 109201.
- Xu, C., Saifullah, S., & Ali, A. (2022). Adnan, Theoretical and numerical aspects of Rubella disease model involving fractal fractional exponential decay kernel. *Results in Physics*, 34, Article 105287.
- Zarei, M., Lee, G., Lee, S. G., & Cho, K. (2023). Advances in biodegradable electronic skin: material progress and recent applications in sensing, robotics, and human-machine interfaces. *Advanced Materials*, 35, Article 2203193.
- Zhai, T., Li, D., Fei, G., & Xia, H. (2015). Piezoresistive and compression resistance relaxation behavior of water blown carbon nanotube/polyurethane composite foam. *Composites Part A: Applied Science and Manufacturing*, 72, 108–114.
- Zhang, B.-X., Hou, Z.-L., Yan, W., Zhao, Q.-L., & Zhan, K.-T. (2017). Multi-dimensional flexible reduced graphene oxide/polymer sponges for multiple forms of strain sensors. *Carbon*, 125, 199–206.
- Zhang, J., Wang, Z., & Peng, Z. (2021). Analytical model of the piezoresistive behavior of highly compressible sensors made of microporous nanocomposites. *Advanced Theory and Simulations*, 4, Article 2100247.
- Zhang, Y., Zhang, T., Huang, Z., & Yang, J. (2022). A new class of electronic devices based on flexible porous substrates. *Advanced Science*, 9, Article 2105084.
- Zhang, J., Wang, Z., Shang, C., Qian, Z., Wu, Z., Yu, X., et al. (2024a). Piezoresistive relaxation and creep model of porous polymer nanocomposite supported by experimental data. *Sensors and Actuators A: Physical*, 366, Article 115002.
- Zhang, X., Sun, Q., Liang, X., Gu, P., Hu, Z., Yang, X., et al. (2024b). Stretchable and negative-Poisson-ratio porous metamaterials. *Nature Communications*, 15, 392.
- Zhao, T., Li, T., Chen, L., Yuan, L., Li, X., & Zhang, J. (2019). Highly sensitive flexible piezoresistive pressure sensor developed using biomimetically textured porous materials. *ACS Applied Materials & Interfaces*, 11, 29466–29473.
- Zhao, W., Wang, Z., Zhang, J., Wang, X., Xu, Y., Ding, N., et al. (2021). Vat photopolymerization 3D printing of advanced soft sensors and actuators: From architecture to function. *Advanced Materials Technologies*, 6, Article 2001218.
- Zheng, Q., Zhou, J. F., & Song, Y. H. (2004). Time-dependent uniaxial piezoresistive behavior of high-density polyethylene/short carbon fiber conductive composites. *Journal of Materials Research*, 19, 2625–2634.
- Zhong-Jie, H., & Gen-Qi, X. (2012). Exponential decay in non-uniform porous-thermo-elasticity model of Lord-Shulman type. *Discrete and Continuous Dynamical Systems - B*, 17(1S) - 1SP - 57, 77.